1-1-2016

Dense Periodical Patterns In Photonic Devices: Technology For Fabrication And Device Performance

Sabarish Chandramohan
Wayne State University,

DENSE PERIODICAL PATTERNS IN PHOTONIC DEVICES: TECHNOLOGY FOR FABRICATION AND DEVICE PERFORMANCE

by

SABARISH CHANDRAMOHAN

DISSERTATION

Submitted to the Graduate School

of Wayne State University,

Detroit, Michigan

in partial fulfillment of the requirements

for the degree of

DOCTOR OF PHILOSOPHY

2016

MAJOR: ELECTRICAL ENGINEERING

Approved By:

_____

Advisor Date

_____

_____

_____

DEDICATION

Dedicated to

My Son, Niranjan, and my wife, Arya

&

My parents, Sudha & Chandramohan

ACKNOWLEDGEMENTS

I would like to express my gratitude to my advisor Dr. Ivan Avrutsky for his advice, guidance and support throughout my research. I would like to thank Dr. Amar Basu, Dr. Mark Cheng, and Dr. Boris Nadgorny for being part of my dissertation committee. I thank Dr. Vladimir Shaleav and Dr. Alexandra Boltasseva from Purdue University for their contribution in investigating the technology for fabrication of sub-micrometer patterns on transition metal nitride. I thank Dan Durisin, William Funk, and Dr. Mark Cheng for their help with FIB in nano-fabrication facility at Wayne State University. I like to thank my colleague Pradeep Kumar for his support and help in the lab.

I thank Dr. Syed Mahmud and Dr. Amar Basu for their advices throughout my PhD study. I thank NSF Center for Photonics and Multiscale Nanomaterials (C-PHOM), Material Research Science, and Engineering Center Program for the support through grant DMR 1120923. I thank Dr. Zhixian Zhou, Madusanka perera and Sagar from Department of Physics at Wayne State University for their help with AFM.

I thank my parents, Sudha Chandramohan, Chandramohan, and my wife, Arya Suresh for their support in all my endeavors. I thank my friends Santhosh and Gopakumar Kamalakshakurup for all their support and encouragement during my difficult times.

PREFACE

In this dissertation, I am reporting the technology for fabricating sub-micrometer dense patterns on hard transition metal nitride such as zirconium nitride using focused ion beam milling and enhancing the sensitivity of an optical miniature spectrometer using a real-time image-processing algorithm.

Chapter 1 gives an introduction reviewing the basic parameters of focused ion beam and how it is used for fabrication on different materials including hard metals and nitrides. It also explains the different platforms of development of optical miniature spectrometers and the need to enhance the sensitivity of such devices.

In Chapter 2, an investigation to find appropriate focused ion beam parameters to fabricate successfully sub-micrometer dense patterns on transition metal nitrides is discussed in detail. Chapter 3 discusses the design of the miniature spectrometer. Chapter 4 explains the real-time image-processing algorithm, which maps the pixel number scale of CMOS image sensor to wavelength spectrum and averages along the arc to collect the light from entire arc to enhance the sensitivity. Chapter 5 discusses various testing methods used to test the sensitivity of miniature spectrometer. Chapter 6 concludes the fabrication procedure as well as the image processing.

Sincerely,

Sabarish Chandramohan

TABLE OF CONTENTS

LIST OF FIGURES

CHAPTER 1: INTRODUCTION

Dense periodical patterns such as gratings allow coupling the light in and out of the waveguide in photonic devices enabling them to be used in variety of applications. In this study, we are reporting the technology for fabricating such gratings on zirconium nitride and a real-time image-processing algorithm for enhancing the performance of a grating based photonic device.

For the fabrication, focused ion beam milling parameters for successful fabrication of dense periodical patterns, such as gratings, on hard transition metal nitride, zirconium nitride are investigated. Focused ion beam (FIB) milling recently has a great deal of attention in nanofabrication because of its advantage of mask less fabrication technique. There are discussions on recent developments in FIB milling, and FIB deposition using different liquid metal ion species (LMIS) along with investigation of different parameters, such as scan method, ion dose, milling rate, ion beam current, dwell time, angle of incidence, beam diameter, beam overlapping etc for fabricating structures and complex patterns on various materials as well as various parameters influencing the milling process [1-2]. FIB milling using gallium (Ga^+) as liquid metal ion source has been used for fabricating Bragg gratings with period 240 nm and length 330 μm on very high index silicon-on-insulator (SOI) optical waveguides with ion beam energy of 30 keV, and beam current of 12 pA [3], and Bragg gratings with period 576 nm, depth 100 nm and length 550 μm on fiber for refractive index (RI) sensing applications with ion beam energy of 30 keV, and beam current of 70 pA [4]. Ga^+ ion FIB milling has been used for fabricating gratings for optical communication applications that includes fabrication of micro gratings of periods 200 nm - 2 μm on optical fiber and fiber mounted on silicon sample with ion beam energy of 30 keV, beam current varying from 30 pA - 1 nA, dwell time of 0.1 μs, beam overlapping 50% and variation of ion dose from 10^{18} - 10^{20} cm^{-2} for wavelength division

demultiplexing [5], fabrication of gratings on optical fiber using different beam limiting aperture sizes, beam current, ion spot sizes, milling sequence, beam overlapping and dwell time for transmitter and receiver modules [6], and fabrication of echelon grating (ion beam energy of 26 keV, dwell time of 2s, 10 scans), crossed grating and circular aperture gratings (ion beam energy of 13 keV, dwell time of 0.66 µs, 2250 scans) on PMMA and fluorinated polyimide for wavelength division demultiplexing [7]. Li *et al* [8] proposed a detailed study by varying ion beam fluence and ion beam current for FIB milling of gratings on fused silica. There has been report of optimization of FIB milling parameters such as ion dose, dwell time and loop number for eliminating sidewall angles in the fabrication of sub-micrometer holes on bulk silicon and silicon-on-insulator (SOI) [9].

FIB milling is widely used to fabricate dense periodical patterns such as gratings, photonic crystals, optical micro-cavities etc on silicon nitride (Si_3N_4) and gallium nitride (GaN) [11-20]. Chaganti *et al* [10] investigated fabrication of gratings on hafnium oxide using Ga^+ ion FIB milling with varying ion beam current, magnification, and depths with dwell time of 1 µs, beam overlap of 50% and material setting for silicon and found good quality gratings for ion beam current of 0.3 nA, magnification 2000x and depth 200 nm along with the optical characterization of milled gratings in the visible spectrum. Zinoviev *et al* [11] reported Ga^+ ion FIB milling of gratings with beam energy 30 keV, beam current 230 pA, different ion doses and varying dwell time to achieve different grating periods on sub-micrometer cantilevers on silicon nitride waveguides along with optical characterization of the milled gratings and the effect of gallium ion implantation on the device performance. Cabrini *et al* [12] reported 30keV Ga^+ ion FIB milling with ion beam current of 100 pA, and ion dose of 0.69 mAs cm^{-2} to mill one dimensional photonic crystals on Si_3N_4/SiO_2 channel waveguides, such as Bragg gratings, Fabry-

Perot micro-cavity, and micro-cavity with optimized mirrors with width of 100 nm and depth of 1 μm along with optical characterization using visible and near infrared ranges. Use of FIB milling for fabricating nanometer pore arrays on thin Si_3N_4 membrane for various applications such as high-throughput DNA sequencing [13-14], sensing and electrochemical studies [15], and fluid separation membranes [16] are reported. Yue *et al* [17] investigated FIB milling with varying dwell time to fabricate nanometer pore arrays on Si_3N_4 with, and without gas-assisted etching, and obtained individual pore diameter of 70 nm with high aspect ratio along with aluminum nitride deposition for narrowing the holes.

Steckl *et al* [18] investigated Ga^+ ion FIB milling with varying ion beam energy from 15 keV - 70 keV, angle of incidence from 0^0 - 30^0, and number of scans from 10-50 with ion beam current of 170 pA, fixed ion dose of 1 x 10^{18} cm^{-2}, and varying dwell time on gallium nitride (GaN) of 20 μm thickness, and on GaN thin films with substrates as sapphire, silicon(Si), silicon carbide (SiC) etc, and obtained highest milling rate of 0.6 $\mu m^3/(nA \cdot s)$ for bulk GaN at beam energy of 50 keV, angle of incidence 30^0 and number of scans 50 along with milling rate of thin films to be 2 - 5 times lower than the bulk and the fabrication of distributed Bragg reflection air/GaN gratings. Ren *et al* [19] reported Ga^+ ion FIB milling with ion beam current varying from 1 pA to 2 nA on GaN for fabricating polishing mirror, tilt mirror and nitride/air distributed Bragg gratings (DBR) mirror with vertical side walls and found milling rate for GaN in the range of 0.6 μm^3/nC - 0.43 μm^3/nC along with study of effect of gallium ion implantation during the milling process. Zhang *et al* [20] reported Ga^+ ion FIB milling with accelerated voltage of 30kV, and ion beam current of 10 pA to 500 pA on GaN-based light emitters for fabricating one-dimensional nitride/air distributed Bragg gratings (DBR) stacks, and two-dimensional photonic octagonal quasi-crystals (8PQCs) with depths of 1.3 μm - 3μm and periods 283 nm and 500 nm.

Study of alternate materials for developing plasmonic devices using transition metal nitrides such as zirconium nitride (ZrN) and titanium nitride (TiN) has been reported recently [21-22]. These materials are harder and CMOS compatible as compared to the noble metals like gold, silver etc. and exhibit plasmonic resonance in the visible and near-infrared ranges [23]. TiN and ZrN have optical properties resembling gold which makes it suitable for applications replacing gold [24]. There have been reports of numerous uses of TiN such as forming epitaxial super lattices resulting in hyperbolic metamaterials [25-26], as plasmonic waveguides [27], as local heating antennas [28], as high temperature metamaterial absorbers and emitters for spectrally selective surfaces [29-30] and colloidal nanoparticles for plasmon enhanced photo catalysis [31].

In this study, an experimental investigation of appropriate FIB milling parameters, such as ion beam current, magnification, beam overlapping, dwell time, and milling rate for fabricating sub-micrometer gratings on zirconium nitride (ZrN) is reported. ZrN is harder than noble metals for example gold, silver etc, and commonly used nitrides like silicon nitride, and gallium nitride. One of the advantages of using FIB milling is the fabrication of grating directly on the surface of the material without the need for mask and photo resist film. FIB milling in ZrN is rarely known as of now.

For the device performance, a real-time image-processing algorithm is developed to enhance the sensitivity of a miniature spectrometer, which is an integrated grating based planar single mode waveguide device. Optical spectroscopy measures the absorption or emission of light based on light-matter interaction. The device which displays the corresponding absorption or emission spectra are generally referred to as spectrometers. Conventional desktop spectrometers use mechanical gratings and slits. Miniature and micro spectrometers are small

dimension devices which are mostly developed using planar waveguides with integrated gratings or other optical devices such as resonators, photonic crystals etc, making them suitable for integration and portability. The quality of an optical spectrometer is defined in terms of its resolving power i.e. resolution.

There are reports of miniature and micro spectrometers developed using various combinations of planar waveguide with integrated gratings such as planar gratings with spherical optics [32-34] , planar imaging gratings [35-39], planar transmission gratings [40] and hybrid grating-Fresnel diffractive optical element [41] etc. These includes planar waveguide grating miniature spectrometer having spectral resolutions of 0.2 nm using f = 14 cm and f = 2 cm lenses, and spectral resolution of 0.3 nm using f = 1 cm lens [32], an aberration correcting planar grating micro spectrometer with high spectral resolutions of 0.7 nm [34], a 35 input optical channel micro-spectrometer with resolution of 0.5 nm in the visible spectrum [35], a planar integrated transmission grating waveguide for broadband spectroscopic analysis [40], an optical spectrometer with hybrid grating-Fresnel diffractive element with a resolution of approximately 1 nm and eliminates the need for spherical and focusing optics for more compact design [41].

Miniature and micro spectrometers are also developed using photonic devices such as integrated filter arrays [42], interferometers [43-44], photonic crystals [45], Fabry-Perot optical resonators [46] etc. and broadband diffractive optics with sensor arrays and tapered hollow Bragg waveguides. There are reports of broadband diffractive optics spectrometer with a specially defined sensor array, which uses a nonlinear optimization method to reconstruct the unknown spectrum [47]. A micro-spectrometer using Bragg reflectors capable of omni-directional collection of out of plane radiation in waveguide cladding, which is tapered and leaky, were reported [48]. Different technologies are implemented in the development of these

miniature and micro spectrometers including MEMS [49-51], and Fourier transforms [52-53]. These devices are developed in ultra-violet, visible, and infrared optical spectral ranges.

The application of optical spectroscopy is extended to different fields of science including biosensors, microbiology, and chemical sensors [54-55]. These applications need high level of sensitivity especially when involving very small amount of analytes. Miniature and micro spectrometers can be used in these applications provided the sensitivity of these devices is appropriate for the application. Thus enhancing sensitivity of an integrated optical device for the spectroscopy of monolayer of molecules becomes critical.

Biosensors and chemical sensors based on optical evanescent field detection utilizing different sensing mechanisms such as refractive index change, absorption, fluorescence etc on different optical platforms, such as waveguides (optical fiber and planar), interferometers etc are discussed [56-62]. There are discussions on optical biosensors utilizing refractive index change as sensing mechanism using different technologies, such as surface plasmon resonance, interferometers, resonant mirror, resonant waveguide grating, planar waveguides, fiber gratings, ring resonators, photonic crystals etc along with comparison of sensitivity based on detection limits of these devices for various proteins, DNAs etc [56-57]. Refractive index sensors detect the resonance change due to change in the effective index of the system by binding of biomoelcules on the sensor surface where as the sensors based on fluorescence measures the photoluminescence intensity [56-62]. Sensors based on absorption measures change in the evanescent field intensity (attenuation of evanescent field) due to absorption by the adsorbed biological or chemical molecules on the sensor surface [56-62]. There are discussions on direct spectroscopic sensors based on fluorescence, absorption, and Raman spectroscopy etc, which utilize the absorption of evanescent field intensity [59, 61]. Bradshaw *et al* [63] reported such a

direct spectroscopic sensor for optical biosensing and chemical sensing for thin films and sub-monolayer for thin film sensing using attenuated total reflectance (ATR) spectroscopy. In this study, a miniature spectrometer that can be categorized as direct spectroscopic absorption sensor that measures the attenuation of evanescent field is proposed. Concept of such a high sensitive device is shown in Figure-1.1.

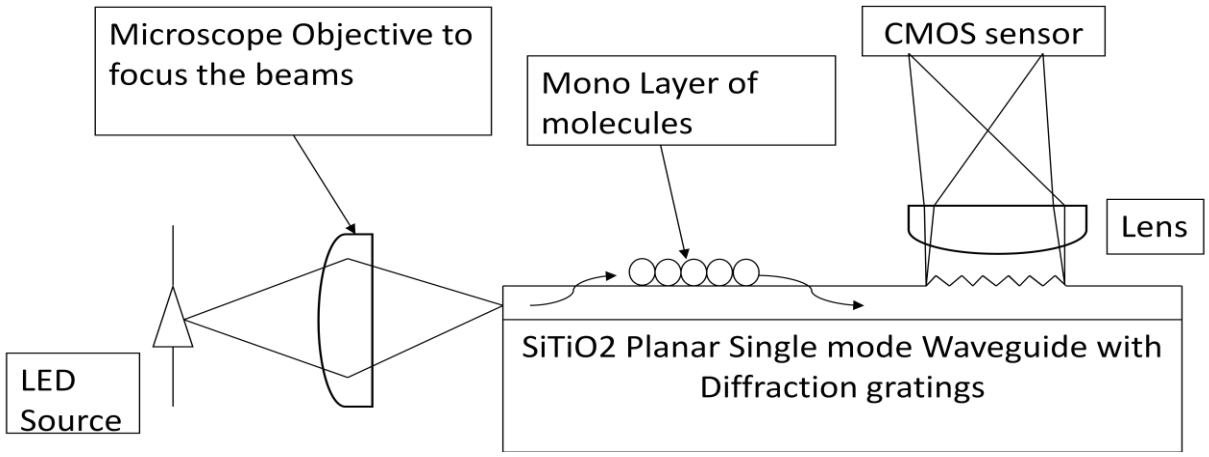

Figure-1.1: An integrated optical device for the spectroscopy of a monolayer of molecules. After Chandramohan *et al* Appl. Spectrosc. **70**, 756-765 (© 2016).

High sensitive spectroscopy involves low signal to noise ratio (SNR) signals or images. This emphasizes the need to use data processing algorithms to process these signals or images to display the spectrum. These data processing algorithms includes least-mean square (LMS) algorithms [64-65], Kalman filtering [66] etc. There are discussions of various methods of deconvolution to reconstruct and optimize the low SNR output signals [67-70]. An algorithm for efficient peak detection in low SNR signals was reported [71]. There are reports of dedicated digital signal processors (DSP) for efficient running of these complex algorithms in real-time [72-73]. The raw data and the spectrum reconstructed using the above-mentioned algorithms are mostly one-dimensional arrays. However, in some optical instruments such as miniature and micro spectrometers, which use image sensors for detection, the raw output is a two-dimensional image. However, the spectrum measured by these devices will still be one-dimensional. Thus,

specialized image processing algorithm has to be developed for the images produced at the image sensor, which takes into account specific features of light intensity patterns of these images. These algorithms will also help to reconstruct the spectra to be measured using these devices.

Here, we report the design of a planar single-mode waveguide miniature spectrometer with a real time image-processing algorithm to enhance the sensitivity in visible spectrum. The image-processing algorithm in this design utilizes a novel approach of averaging the intensity distributions of the monochromatic inputs along the arcs registered on the image sensor. Thus enhancing the sensitivity by collecting more light and retaining the spectral resolution of the miniature spectrometer defined by a single row of pixels. Standard built-in Matlab functions such as 'findpeaks' [74] for finding the laser peaks as well as its central pixel numbers and 'lsqcurvefit' [75] for curve fitting are used for demonstrating the concept. The proposed algorithm is illustrated using a $SiTiO_2$ planar waveguide miniature spectrometer with core index of 1.77 and the sensitivity of the device is demonstrated using a tantalum pentoxide (Ta_2O_5) planar waveguide with higher core index of 2.16, providing stronger light confinement, thus stronger light-matter interaction at the waveguide surface. Properties of Ta_2O_5 films and their applications for evanescent field based sensors are discussed in [76]. The proposed algorithm can also be used along with various deconvolution and digital filtering methods reported elsewhere. Comparison of sensitivity with the known devices is discussed in chapter 5.

CHAPTER 2: INVESTIGATION OF FIB PARAMETERS FOR SUCCESSFUL FABRICATION OF DENSE PATTERNS

FIB parameters for successful fabrication of dense patterns on transition metal nitride such as ZrN are investigated using 30 keV Ga^+ ion Tescan GAIA 3 dual beam FIB/SEM. Using dual beam FIB/SEM allows for real-time monitoring of FIB milling. Successful fabrication of dense patterns on this novel transition metal nitride such as zirconium nitride requires milling parameters to be set appropriately. Ion beam current, magnification, dwell time and the milling rate are the few of the important parameters investigated in this study. The patterns used in this study are gratings. Design of dense patterns to be milled are achieved using Drawbeam, which is the lithography software provided by the manufacturer Tescan. The milling rates for common materials such as silicon, copper, iron, silver etc. are available in Drawbeam.

The procedure for investigation of FIB parameters is as follows. Gratings are fabricated on ZrN using the milling rates for the common materials already given by the manufacturer in the software and some manually inputted rates. The gratings are then characterized using AFM to determine the depth of the milled grating. The actual milled depths of the fabricated grating for the set milling rates are thus obtained. Using this data, the actual milling rate is then calculated.

The design of the gratings to be fabricated on ZrN is described below. The grating period is set at 540 nm, the width of the grating's groove to be milled is set at 200 nm, the length of each grating's groove is set at 50 µm, and the depth to be milled is set at 50 nm. Since the purpose of fabricating these gratings is to find the appropriate parameters, few grooves of grating are only needed and so the number of grooves of grating is set to 10. The grating profile is chosen to be rectangular in this design.

The parameters beam spacing and object order also plays vital role in the milling procedure. The successful fabrication of grating depends on the appropriate setting of these parameters. The beam spacing determines the degree of overlapping of FIB beam and the object order provides the order of milling each object in the design. The degree of redeposition of materials during milling process depends on the object order used. In this study, the beam spacing is set to 0.1, which provides 90% overlap of the ion beam. The object order is set to parallel which helps to reduce the redeposition. Even though rectangular profile is chosen in this design, the grating profile after milling looks more smooth like sinusoidal. This may be due to the Gaussian nature of the ion beam used for milling.

2.1 Ion beam current

Ion beam current is an important parameter governing the successful milling of dense patterns especially in the sub-micrometer dimension. The size of the aperture in the FIB ion column is adjusted in order to obtain different ion beam currents. Large current requirement leads to larger aperture size which results in the large spot size of the ion beam on the sample surface.

In the case of dense periodical patterns such as gratings in sub-micrometer dimension, large beam current will result in the overlapping of grating's grooves. Different ion beam currents are chosen ranging from the minimum beam current of 4 pA to larger currents. The grating fabricated with ion beam current of 153 pA resulted in overlapping of grating's grooves as shown in Figure-2.1. Thus, the appropriate ion beam current for fabricating gratings of 540 nm dimension on ZrN is found to be about 50 pA or less. The ion beam current needs to be decreased in the case of smaller dimension patterns to avoid overlapping.

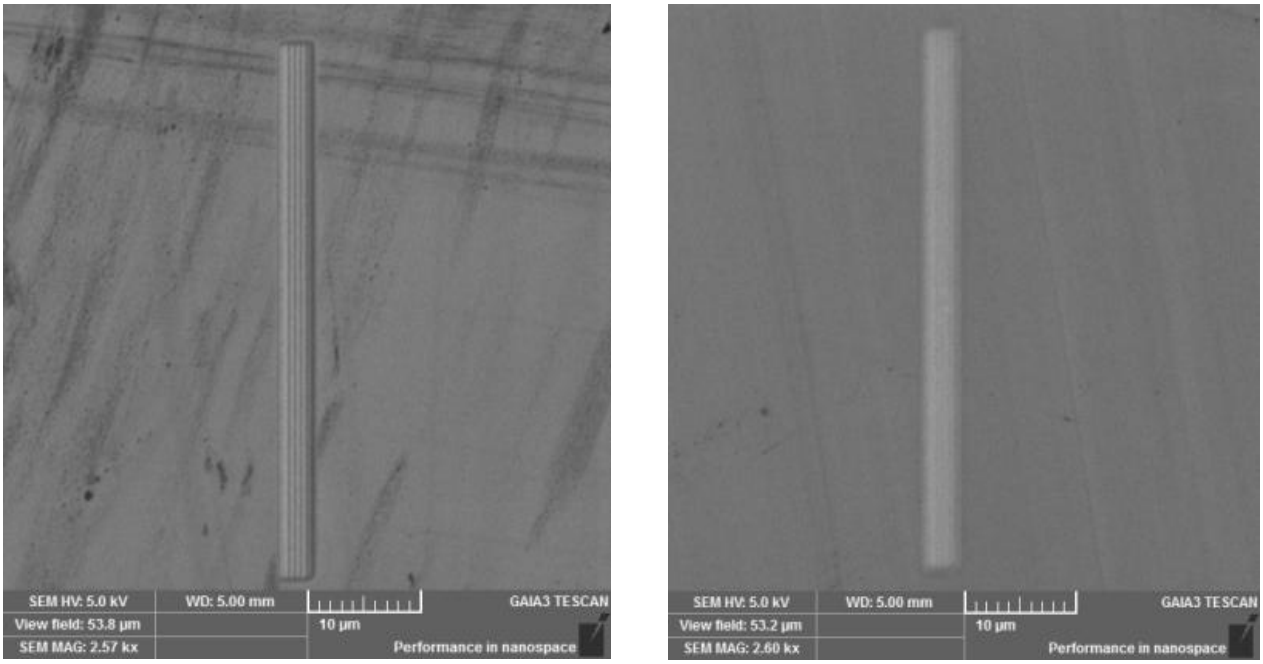

(a) (b)

Figure-2.1: SEM image of gratings milled on ZrN using FIB currents (a) 50 pA (b) 153 pA.

2.2 Magnification

Magnification of FIB view field is another important factor governing the quality of milled dense patterns. Appropriate magnification needs to be set depending on the actual dimensions of the patterns to be milled. The rule of thumb is to set a magnification so that the pattern to be milled is quite magnified within the view field. In this study, since the length of the grating is chosen to be 50 µm, FIB magnification is set at 2000 x (2 kx), which provides a view field of about 63 µm. Smaller dimension patterns require the magnification to be increased appropriately.

2.3 Dwell time

The time for which the ion beam remains at a given pixel is generally referred to as dwell time. Dwell time plays a vital role in the FIB milling process as this factor determines the exposure of a particular location of the sample area to be milled and the scanning speed of the ion beam. Increase in dwell time can result in increased exposure and could result in higher

milled depth than desired. In this study, the gratings are fabricated using dwell times of 1 µs, 5 µs, 10 µs, and 15 µs.

2.4 Milling rate

The volume of material sputtered per nA of ion beam current for a given time of exposure is commonly referred to as milling rate. The unit of milling rate is μm^3/ (nA·s). The general expression for milling rate is given in Eq. (1).

$$R = \frac{d.A}{I.\,t} \tag{1}$$

Here *d* is the set depth i.e. the depth to be milled in µm, *A* is the area of the designed pattern to be milled in μm^2, *I* is the ion beam current in nA and *t* is the time of exposure in seconds.

The amount of material milled from a particular area is determined by Ion dose. Ion dose is generally defined as the amount of ions hitting per μm^2 of sample area for the given time of exposure. The unit of Ion dose is (nA·s)/μm^2. The general expression for Ion dose is given in Eq. (2).

$$D = \frac{I.\,t}{A} \tag{2}$$

We can infer from Eq. (2) that the increase in the time of exposure results in increased ion dose. The milling rate is related to ion dose given in Eq. (3). Since the ion dose is inversely proportional to the milling rate and assuming the milling depth is constant, increasing ion dose will result in decreased rate of milling.

$$R = \frac{d}{D} \tag{3}$$

In FIB, the milling rate has to be set correctly in order to reach the desired set depth. Since milling rate for zirconium nitride is unknown, the values we set as milling rate to fabricate the gratings can be called manual milling rate, denoted by *S*. Here *S* represents the milling rate of common materials and some manually set milling rate used to fabricate the gratings on ZrN to find the actual milling rate. Therefore, the milling rate R in Eq. (1) is replaced by *S*. By setting *S*, we are actually controlling the time of exposure of milling. Thus, the time of exposure can be defined in terms of S and Eq. (1) can be rewritten as given in Eq. (4). Setting the defined manual rate, *S* to too high or too low value would result in brief or excessive exposure of the milling pattern and results in too shallow or too deep structure.

$$t = \frac{d.A}{S.I} \tag{4}$$

Gratings are fabricated on ZrN by setting S to 0.24 μm^3/ (nA·s) (rate for silicon), 0.36 μm^3/ (nA·s) (rate for copper), 0.608 μm^3/ (nA·s) (rate for iron), 1.105 μm^3/ (nA·s) (rate for silver) etc. An arbitrary value of 0.1 μm^3/ (nA·s) is also chosen along with the above mentioned milling rates. From Eq. (4), the time of exposure is calculated for these set values of *S* for the set depth of 50 nm. This calculated time of exposure is then substituted in Eq. (2) to calculate the ion dose, which provides the ion dose for different values of *S*. This calculated ion dose along with the milled depth from AFM profiles is substituted in Eq. (3) to calculate the actual milling rate for ZrN as explained below. The actual milled depth of the gratings fabricated on ZrN is determined using AFM. AFM profiles are obtained for the gratings fabricated using all the *S* values. AFM profiles of gratings fabricated on ZrN for milling rates of 0.1 μm^3/(nA·s), 0.24 μm^3/(nA·s) and 0.36 μm^3/(nA·s) are shown in Figure-2.2.

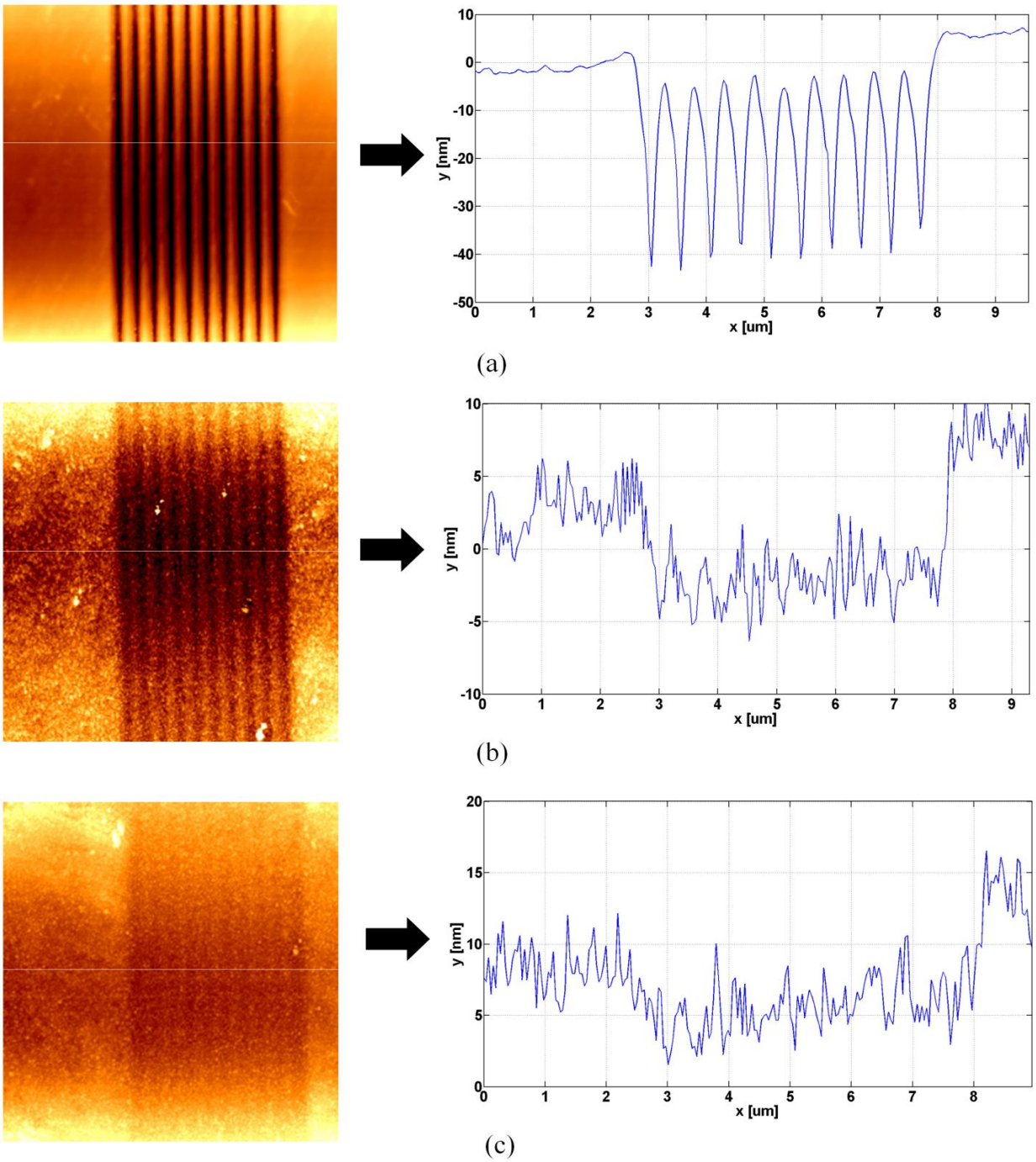

Figure-2.2: AFM topography and cross section profile of grating fabricated using manual milling rates, *S* (a) 0.1 $\mu m^3/(nA \cdot s)$, (b) 0.24 $\mu m^3/(nA \cdot s)$ and (c) 0.36 $\mu m^3/(nA \cdot s)$ for the dwell time of 1 µs.

From Figure-2.2 (c), grating's grooves can be barely observed on the AFM profile of grating fabricated using the *S* value of 0.36 $\mu m^3/ (nA \cdot s)$. Therefore, it can be concluded that the

higher milling rates for iron and silver will not be sufficient to produce an observable grating in this hard transition metal nitride. The surface roughness in Figure-2.2 (b) and (c) is not as smooth compared to Figure-2.2 (a). This is because of the difference in the substrate on which the ZrN film is deposited. The surface roughness is observed to be high for silicon substrate and almost negligible for magnesium oxide (MgO) substrate.

The actual milling rate is determined by substituting the milled depth obtained from AFM profiles and the calculated ion dose, D in Eq. (3). The milled depth obtained from AFM is plotted against the ion dose calculated for the *S* values of 0.1 μm^3/ (nA·s), 0.24 μm^3/(nA·s) and 0.36 μm^3/(nA·s) for all dwell times as shown in Figure-2.3.

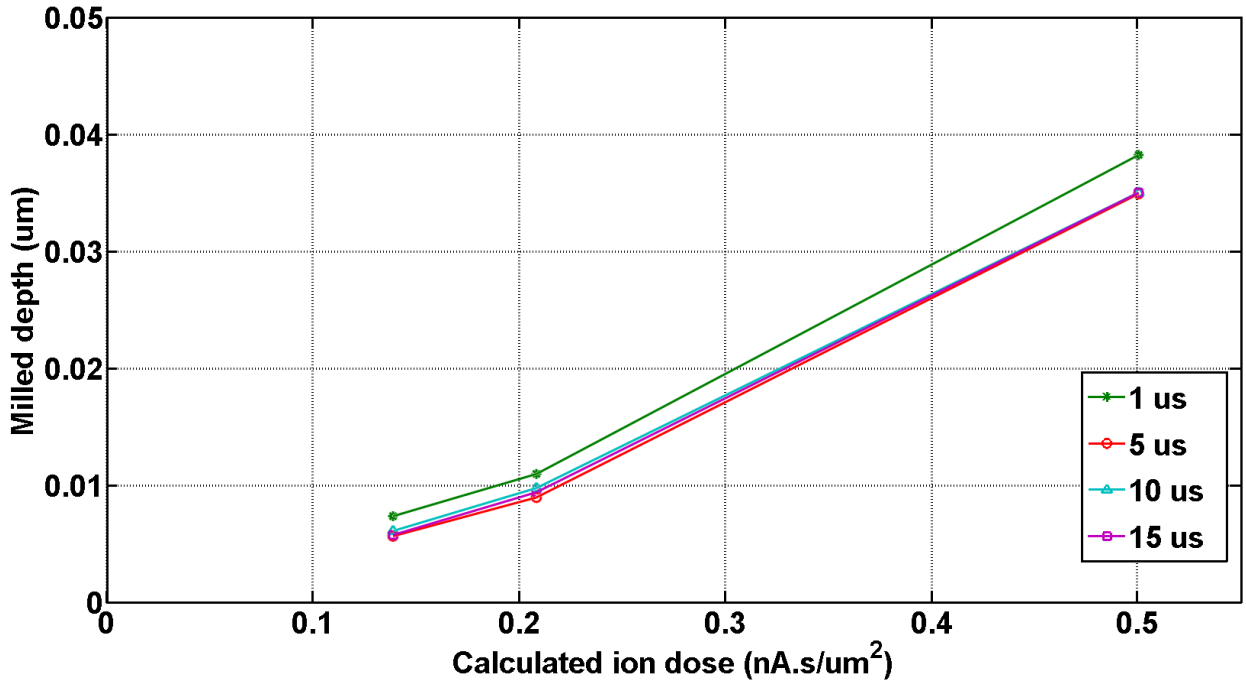

Figure-2.3: Milled depth versus calculated ion dose

Since from Eq. (4), the time of exposure decreases as the *S* values increases, the highest calculated ion dose in the Figure-2.3, corresponds to the lowest *S* value. From Figure-2.3, the actual milled depths for the *S* value of 0.1 μm^3/ (nA·s) is 38 nm for dwell time of 1 µs and 35 nm

for dwell times of 5 µs, 10 µs and 15 µs. The milled depths for *S* values of 0.24 μm^3/ (nA·s) and 0.36 μm^3/(nA·s) are observed to be smaller in the range about 10 nm.

Substituting these values of milled depths and the corresponding calculated ion dose from Figure-2.3 in Eq. (3), the actual milling rate, *R* for ZrN is found to be 0.076 μm^3/(nA·s) for dwell times of 1 µs and 0.07 μm^3/(nA·s) for dwell times of 5 µs, 10 µs and 15 µs.

2.5 Testing the accuracy of the found milling rate

The accuracy of the milling rate found is verified by fabricating rectangular gratings on ZrN using 0.07 μm^3/ (nA·s) for dwell time of 5 µs. The period of grating used is 500 nm. The milling depth is set to 50 nm. SEM image and AFM profile of the fabricated grating is shown in Figure-2.4.

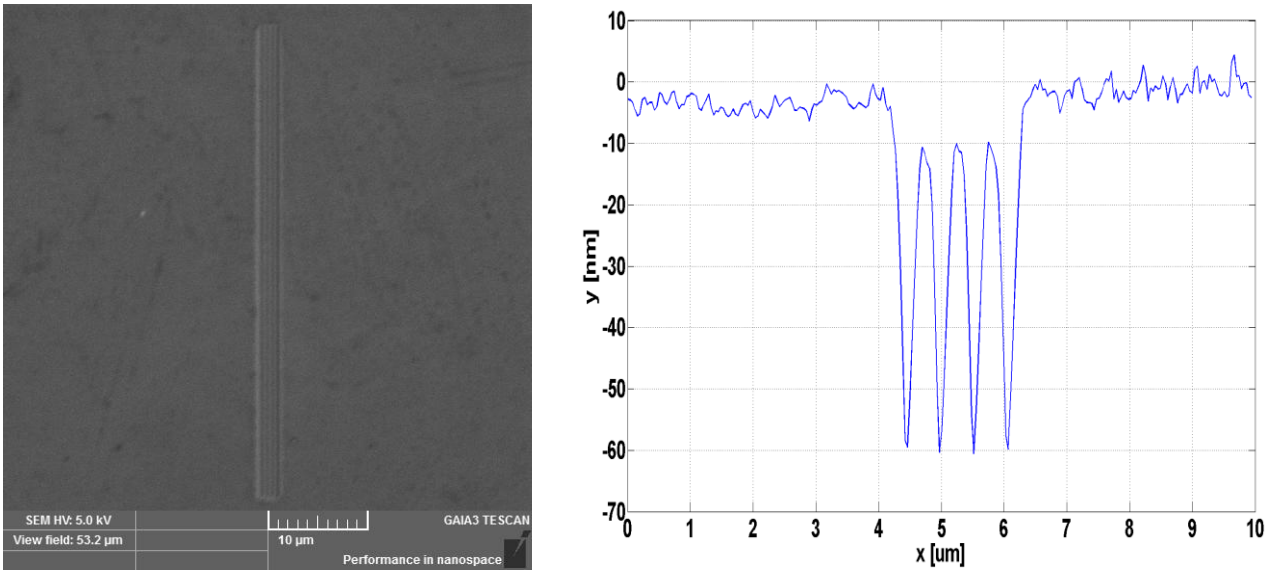

(a) (b)

Figure-2.4: (a) SEM image of grating fabricated on ZrN using milling rate of 0.07 μm^3/(nA·s), (b) AFM profile of grating fabricated on ZrN using milling rate of 0.07 μm^3/(nA·s).

From Figure-2.4, the milled depth obtained from AFM profile is found to be 50 nm, which was the set depth. Thus verifying the accuracy of the actual milling rate for ZrN.

CHAPTER 3: DESIGN OF MINIATURE SPECTROMETER

The basic design of planar single-mode waveguide miniature spectrometer consists of $SiTi0_2$ planar single-mode waveguide with integrated diffraction gratings on a BK7 substrate (waveguide sample) from MicroVaccum [77], a lens to focus the diffracted wavelengths and a CMOS sensor from Aptina to capture the diffracted light. Two known visible wavelengths, green (532 nm) and red (632.8 nm) are used as input to the miniature spectrometer.

3.1 $SiTi0_2$ planar single-mode waveguide on BK7 substrate

The $SiTi0_2$ planar single-mode waveguide has dispersive diffraction gratings integrated on the waveguide film. The refractive index of the $SiTi0_2$ waveguide film dependents on the wavelength and polarization of the guided light. According to the data provided by manufacturer [78], modal index at the wavelength of 633 nm is 1.778 for TE polarization and 1.775 for TM polarization. The modal index at the wavelength of 514 nm is 1.808 for TE polarization and 1.801 for TM polarization. The BK7 glass substrate [79] has refractive index of 1.5195 at 532 nm and 1.5151 at 633 nm. The thickness of the $SiTi0_2$ film is 200 nm. The grooves of diffraction grating have surface relief structure of 20nm. The periodicity of the grating is 2400 lines/mm, which corresponds to a period of 416.6 nm. The total width of grating is 2 mm. The grating grooves are parallel to the width of the sample.

3.2 CMOS image sensor

The CMOS image sensor used in this design is Aptina MT9M032 monochromatic sensor. The sensor area is 3.24 mm x 2.41 mm. The pixel size is 2.2 µm x 2.2 µm. It is a 1.6 Mp image sensor with maximum image size of 1440 x 1080 with optical format of 1/4.5 inch (4:3). The output of the sensor is set to maximum bit-size of 12-bit and the filter array format used is Bayer pattern (Bayer-12). The sensor board is attached to a Demo Board from Aptina, which can be connected to the PC through USB port.

3.3 Lens

The choice of the lens in the miniature spectrometer depends on the period of the integrated grating in the waveguide used and the CMOS sensor area. Since the CMOS sensor area is small in this design, if the period of the grating is close to half of the input wavelengths, the divergence of the light will be more requiring lens with smaller focal length for the diffracted wavelengths to be captured by the CMOS sensor. However, if the period of grating is three by fourth of the input wavelengths, lens with larger focal length can be used. Since the period of grating of the $SiTi0_2$ planar single-mode waveguide is 416.6 nm, which is close to three by fourth of input wavelengths used, lens with focal length of 1cm is chosen.

3.4 Optical miniature spectrometer

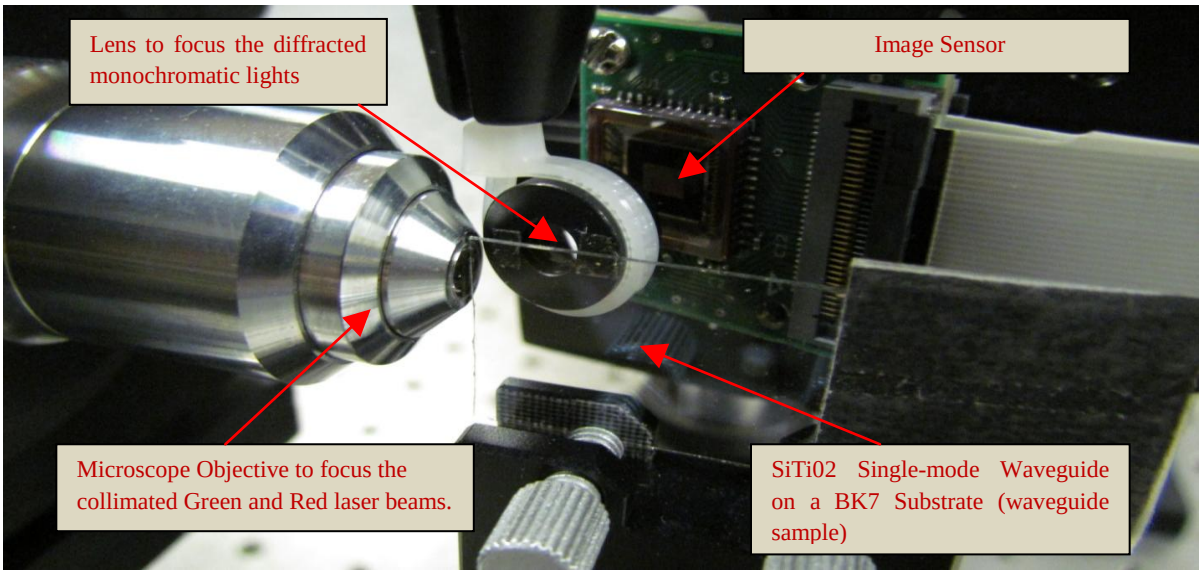

Figure-3.1: Setup of optical miniature spectrometer in the optical table. After Chandramohan *et al* Appl. Spectrosc. **70**, 756-765 (© 2016).

Planar single-mode waveguide optical miniature spectrometer assembled in optical table is shown in Figure-3.1. The light is delivered to the miniature spectrometer using a single-mode fiber. The light path design is described below. Two visible monochromatic lasers with wavelengths, green (532 nm) and red (632.8 nm) are combined using a beam splitter and

delivered to a single-mode fiber with collimator. The same collimator is used at the other end of the single-mode fiber to deliver the light to the miniature spectrometer setup. The use of single-mode fiber in the design provides spatial filtering for the input monochromatic lights. The collimated monochromatic light out coupled from the single-mode fiber is passed through a quarter-wave plate before the miniature spectrometer to compensate for any polarization effects introduced by the fiber. The monochromatic light after the quarter wave plate is focused by a microscope objective onto the edge of the $SiTi0_2$ planar single-mode waveguide of the waveguide sample. The waveguide sample is mounted on a three-way translational stage, providing the waveguide movement in X, Y and Z directions to the input monochromatic wavelengths focused by the microscope objective, thereby allowing for optimized coupling. Additional adjustment is possible with the microscope objective in X, Y and angular directions that allows the movement of the input light focus as well.

Since we are developing an algorithm to make this device highly sensitive and the CMOS image sensor used in this design are very sensitive, laser beams needs to be attenuated before they are coupled to the fiber. Separate attenuation is needed for the green and red laser beams as they have different levels of output power. The collimated green and red monochromatic laser beams after guided through the planar waveguide film are diffracted at different angles by the integrated gratings and are focused by the lens onto the CMOS image sensor. The larger wavelength of red monochromatic light accounts for smaller diffraction angle and thus is registered to the lower *x*-pixel number region of the CMOS image sensor. The green monochromatic light on the other hand having smaller wavelength than red monochromatic light diffracts at a larger angle and is registered to the higher *x*-pixel number region of the CMOS image sensor. Figure-3.2 shows the diffracted green and red monochromatic lights registered on

the CMOS image sensor. The horizontal direction in the figure corresponds to the *x*-pixel number and the vertical direction corresponds to the *y*-pixel number of the CMOS image sensor.

Figure-3.2: Diffracted green and red monochromatic lights registered on CMOS image sensor (the image shows different aspect ratio as it is rescaled in the vertical direction).

From Figure-3.2, the registered diffracted images are discontinuous arcs rather than straight lines. This can be mainly due to the monochromatic light being diverged in the plane of the waveguide film. Other factors such as barrel distortion, introduced by the use of spherical lens with small diameter can also be contributing to the arc shaped images. The image-processing algorithm developed does not rely on particular factor contributing to the arc shaped images and quantifies for the curvature of these arcs.

We used a polarizer to verify that the light reaching the image sensor is in fact the diffracted images due to the guided mode and not the stray light scattered from the glass substrate. The polarizer was placed before the microscope objective. Only TE or TM modes, or mixture of both can be excited by setting the polarizer at different angles as shown in Figure-3.3 (a), (b) and (c). As the modal index in a planar waveguide depends on polarization, so does the location of image on the sensor. From this, we can conclude that the image registered on the CMOS image sensor is evidently the diffracted light and not the scattered stray light. In Figure-3.3 (c), the image sensor is shifted towards left to capture the TM component of red

monochromatic input. In this study of miniature spectrometer, we chose to work with TE-polarized mode.

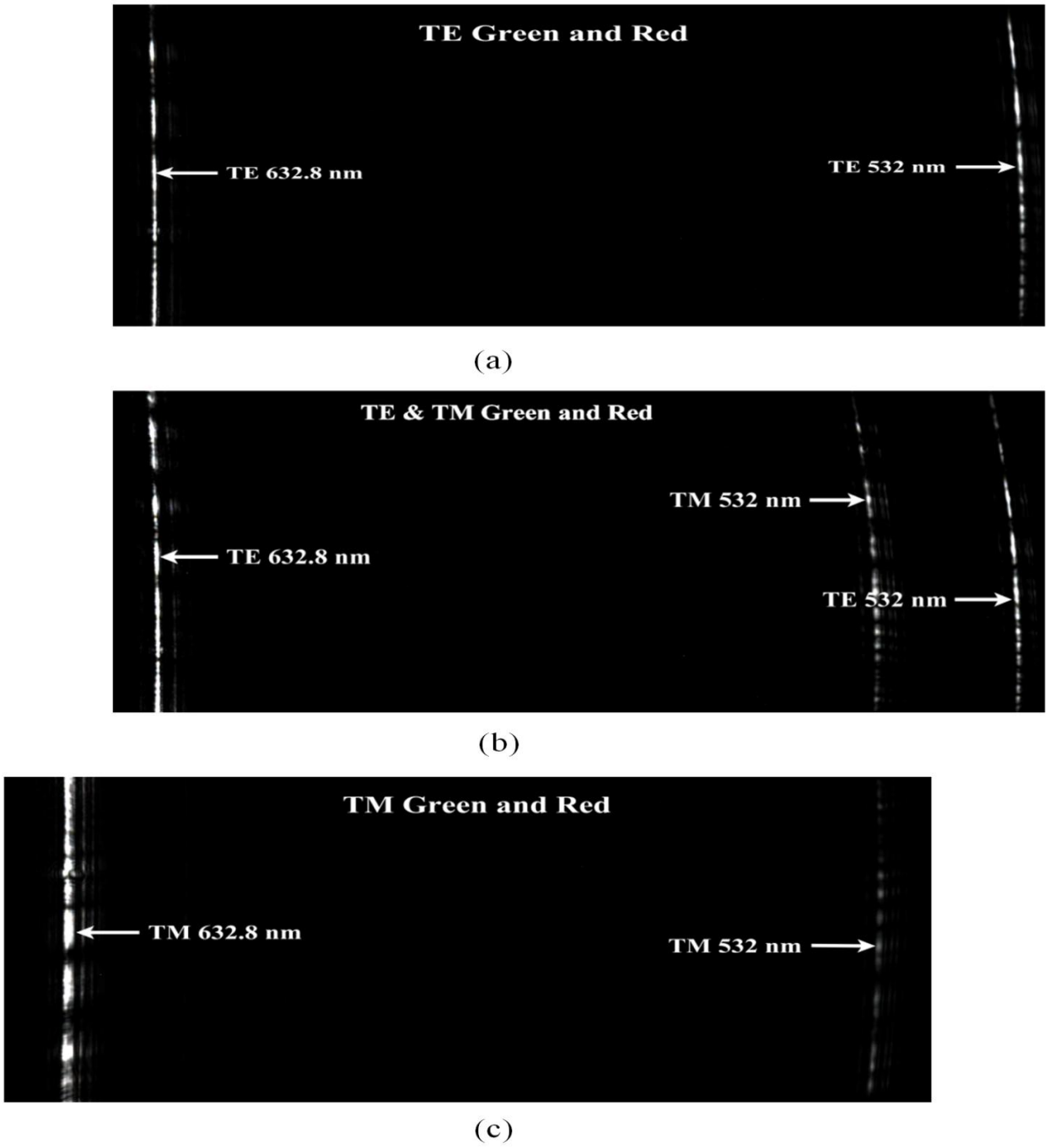

Figure-3.3: (a) TE-polarized images of green and red monochromatic inputs, (b) TE&TM polarized mixed images of both monochromatic inputs, (c) TM-polarized images of green and red monochromatic inputs (physical shifting of image sensor towards left direction was needed for capturing signals produced by TM-polarized inputs).

Chapter 4: REAL-TIME IMAGE-PROCESSING TO ENHANCE THE SENSITIVITY OF MINIATURE SPECTROMETER

The sensitivity of the miniature spectrometer is enhanced in this design using a real-time image-processing algorithm. We have chosen Matlab to implement the algorithm. The sensitivity enhancement is achieved by averaging along the arc shaped images registered on the CMOS image sensor. This helps to collect the light from the entire arc to display the spectra. Averaged intensity displayed with respect to the wavelength spectra is the final output of the algorithm, which is the desired spectrum displayed by the miniature spectrometer.

The CMOS image sensor used in this design produces an output of two-dimensional array of data. This data represents the registered light intensity with respect to the *x*- and *y*-pixel numbers of the image sensor. The algorithm developed in this design works in two modes, the calibration mode, and the measurement mode. The main function of algorithm in calibration mode is to map the two-dimensional pixel array of CMOS image sensor to the wavelength spectra using the two known monochromatic sources of light inputs. The algorithm in measurement mode uses the already calibrated data and does the averaging along the arcs in real-time to display the output of the miniature spectrometer. So in order to use the measurement mode of the algorithm, calibration mode needs to be executed first.

Due to the divergence of light in the plane of the waveguide, the diffracted images of green and red monochromatic inputs as well as for any other monochromatic inputs registered on the CMOS image sensor are shaped as arcs. Therefore, an appropriate mapping scheme needs to be implemented which can assign all the pixels along a given arc to the corresponding wavelength. A curved coordinate system is used in this algorithm to achieve the averaging along the arcs. This novel approach helps to enhance the sensitivity of the miniature spectrometer by collecting light from the entire arc.

The interfacing of CMOS image sensor software, DevWare [80] to Matlab is achieved using actxserver [81] in Matlab. Real-time raw images from DevWare are taken using actxserver and the averaging along the arcs is done using the algorithm to display the output of the miniature spectrometer. The real-time processing helps to observe the instantaneous changes in the CMOS sensor output.

4.1 Calibration mode

The *x*- and *y*-pixel numbers of CMOS image sensor are mapped to the wavelength spectra using the calibration mode. Two monochromatic sources with known wavelengths are used as inputs to the miniature spectrometer during the calibration procedure. The mapping can be subdivided into three phases that are image acquisition phase, curve fitting phase and mapping phase.

4.1.1 Image acquisition phase

Raw images from CMOS image sensor is captured in real-time during this phase of the calibration mode. Invoke function in actxserver is used to get the raw images from Devware, the CMOS image sensor software.

4.1.2 Curve fitting phase

The curve fitting helps to determine the accuracy of the central *x*-pixel numbers found by the 'findpeaks' function and correct the data if needed. The least square curve fitting method is used in this algorithm to fit the original data with a non-linear Gaussian curve function. Error is minimized in this least square method by determining the square of the difference between the fitting data and the original data.

In the curve-fitting phase, the algorithm scans the incoming raw images to find the bright *y*-pixels for both green and red discontinuous arcs. The intensity versus *x*-pixel numbers data are

generated for these bright *y*-pixels by selecting a single *y*-pixel (represented by the red line) from the diffracted images registered on the CMOS image sensor as shown in inset of Figure-4.1(a). The 'findpeaks' function in Matlab is then used on this intensity versus *x*-pixel numbers data to find the maximum intensity peaks for green and red monochromatic inputs as well as central *x*-pixel numbers for these maximum intensities.

The 'lsqcurvefit' function in Matlab is used in this phase for curve fitting. The inputs to 'lsqcurvefit' function are a non-linear Gaussian function saved as matlab function file, the intensity profile of bright *y*-pixel numbers and *x*-pixel numbers of CMOS image sensor. The inputs to the Gaussian function generated using Matlab are the central *x*-pixel numbers for both green and red arcs, curve widths and *x*-pixel numbers of CMOS image sensor. Two Gaussian curves are added together and used to fit the original data since two monochromatic sources are used as inputs in the calibration mode. Corrected central *x*-pixel numbers are obtained from the output of the lsqcurvefit function. The parameters *a* and *b* defined in Eq. (1) in the mapping phase, needed to find the relation between wavelength spectrum and *x*-pixel numbers is evaluated using this corrected central *x*-pixel numbers. Figure-4.1 shows curve fitted intensity peaks for both green and red monochromatic inputs versus *x*-pixel numbers. From Figure-4.1 (b) and (c), one can notice that the red monochromatic input is diffracted at smaller angle with respect to the normal of the grating and gets registered on lower *x*-pixel number region of CMOS image sensor and green with higher diffraction angle, gets registered on higher *x*-pixel number region of CMOS image sensor.

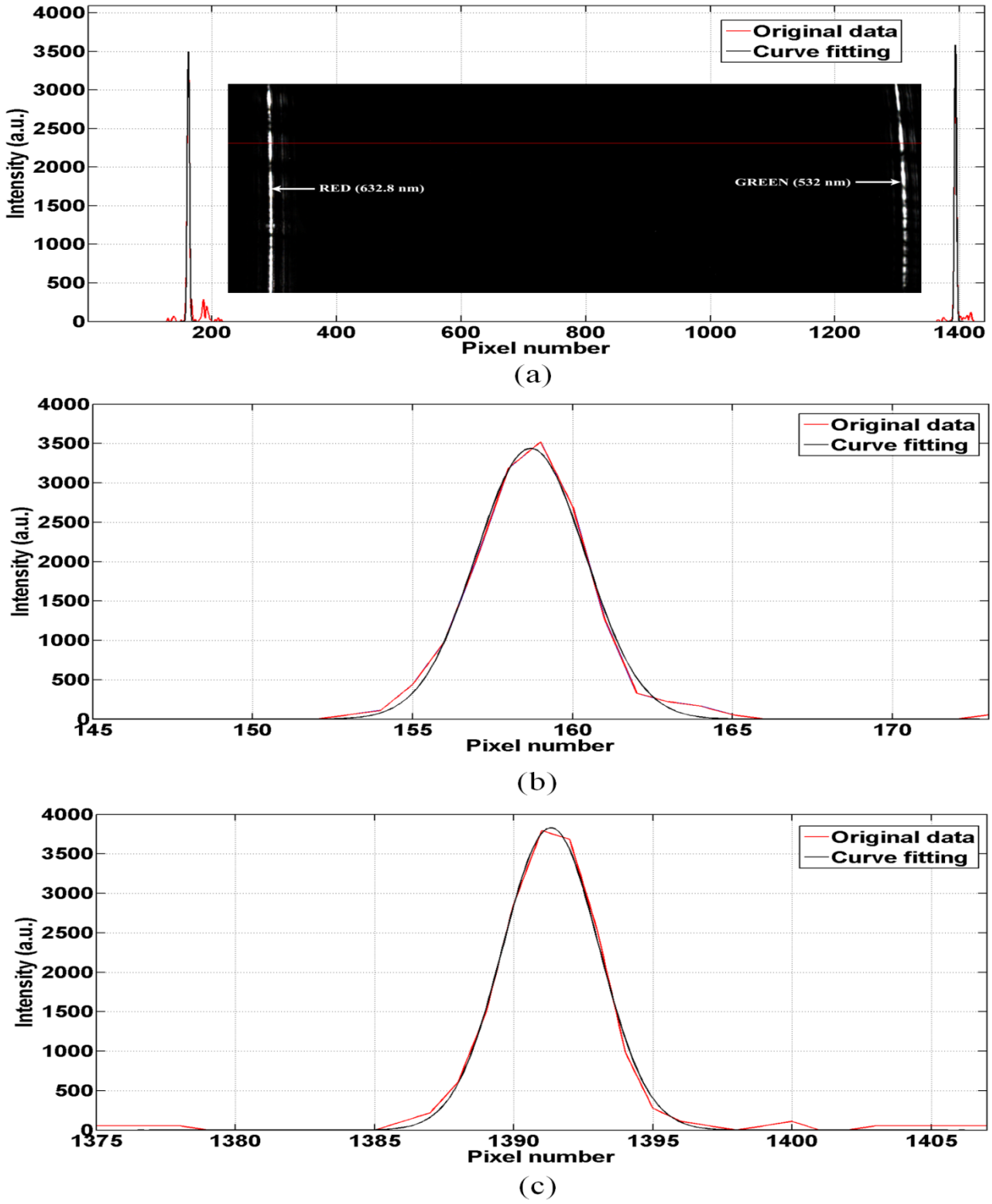

Figure-4.1: (a) Curve fitting using 'lsqcurvefit' for a single bright *y*-pixel line (inset: diffracted green and red monochromatic lights registered on CMOS image sensor (image is rescaled) and red line indicates a single *y*-pixel line), (b) Close view of red monochromatic input curve fitting, (c) Close view of green monochromatic input curve fitting. After Chandramohan *et al* Appl. Spectrosc. **70**, 756-765 (© 2016).

4.1.3 Mapping phase

Overview of the entire mapping scheme is described here. The relation between wavelength, λ and *x*-pixel number of the CMOS image sensor is assumed a linear function defined by two parameters *a*(*y*) and *b*(*y*) for each bright *y*-pixels selected. Second-order curves are then used to approximate the *y*-dependence of *a* and *b*. This approximation requires sets of three constants (*c*, *d*, *g*) for parameter *a* and (*p*, *q*, *r*) for parameter *b*. These six constants are then used to calculate the values of *a*(*y*) and *b*(*y*) for entire array of *y*-pixels. Wavelength grid, λ_i is chosen independently. The set of *x*-pixels is then calculated for each wavelength in the wavelength grid, λ_i. Implementation of a curved coordinate system that transforms (*x*, *y*) coordinates of pixels into (λ_i, *y*) coordinates are achieved using this mapping scheme. Since the arcs in the diffracted image represents a single wavelength, the arcs become straight lines in the (λ_i, *y*) coordinate system. Detailed implementation of the mapping scheme is described below.

Two-point form of line equation is used to define the linear relation between λ and *x*-pixels shown in Eq. (5).

$$\lambda(x) = \lambda_1 + \frac{(\lambda_2 - \lambda_1)}{(x_2 - x_1)}(x - x_1) = \frac{(\lambda_1 x_2) - (\lambda_2 x_1)}{(x_2 - x_1)} + \frac{(\lambda_2 - \lambda_1)}{(x_2 - x_1)}x = a + bx \tag{5}$$

Here, $a = \frac{(\lambda_1 x_2) - (\lambda_2 x_1)}{(x_2 - x_1)}$ and $b = \frac{(\lambda_2 - \lambda_1)}{(x_2 - x_1)}$.

The linear relation between wavelength and *x*-pixel numbers is justified by calculating the dispersion along the *x*-pixel numbers of the image sensor for which, we have chosen a simple design without lens. The image sensor pixel coordinates *X* for the corresponding values of wavelength λ is calculated using Eq. (6).

$$X(\lambda) = \mathrm{h}\frac{(\mathrm{n}_{\mathrm{eff}}(\lambda) - (\lambda/\Lambda))}{\sqrt{1-(\mathrm{n}_{\mathrm{eff}}(\lambda) - (\lambda/\Lambda))^2}} \tag{6}$$

Here h is the distance between grating and the image sensor, n_{eff} is the effective index for TE polarization, λ is the wavelength, Λ is the period of the grating.

From Eq. (6), wavelength versus *x*-pixel numbers for the entire visible spectra is plotted. It is observed to be linear. The slope of the line, which gives the dispersion along the *x*-pixel numbers of the image sensor, was calculated for both green and red monochromatic inputs. The slope at green monochromatic input, 532 nm is found to be -0.079 nm per pixel and slope at red monochromatic input, 632.8 nm is found to be -0.092 nm per pixel. Thus linear approximation for $x(\lambda)$ is justified as the change in slope is small enough.

The accuracy of mapping from *x*-pixel numbers of the image sensor to the wavelength scale of the miniature spectrometer will be affected by the nonlinearity of $x(\lambda)$ dependence. However, the nonlinearity is negligible within about 100 nm wide wavelength range of interest as observed from the dispersion calculation. Better accuracy can be achieved in the calibration procedure by involving more than two monochromatic sources. Then higher order polynomial approximation is needed for $x(\lambda)$ dependence.

A polynomial relation is formulated between *a* and *y*, *b* and *y*, and are given by Eq. (7) and Eq. (8).

$$a = a(y) = cy^2 + dy + g \tag{7}$$

$$b = b(y) = py^2 + qy + r \tag{8}$$

The parameters *a* and *b* defined in Eq. (5) are calculated using the two known input wavelengths and the corrected central *x*-pixel numbers for those wavelengths for each selected

bright *y*-pixels from the curve fitting phase. Using the values of *a* and *b* for these known wavelengths and the 'polyfit' [82] function of Matlab, the values of the coefficients (*c, d, g*) and (*p, q, r*) is found. Then values of *a* and *b* for entire 1080 *y*-pixels are found from these coefficients by substituting them in the same polynomial relation given in Eq. (7) and Eq. (8). By knowing the values of *a* and *b* for entire 1080 *y*-pixels, Eq. (5) can be rewritten as:

$$\lambda(x,y) = a(y) + b(y)\,x \tag{9}$$

To improve the accuracy of the mapping, the number of divisions in the wavelength spectrum is intentionally chosen to be higher than the number of *x*-pixels of the CMOS image sensor. The wavelength spectrum is chosen to have 2330 equal divisions starting from λ_{min}, 527.4 nm found by putting 1 for x_{min} and λ_{max}, 644.4 nm by putting 1440 for x_{max} (where 1440 is the highest *x*-pixel number of the CMOS image sensor) in Eq. (9). There is no improvement in the spectral resolution of the miniature spectrometer by setting higher number of divisions in the wavelength spectrum than the number of *x*-pixels of the image sensor; rather it helps to produce a smoother output spectrum.

Since the diffracted images of the green and red monochromatic inputs are shaped as arcs, each wavelength is represented by a set of *x*-pixel numbers rather than a single *x*-pixel number. The set of *x*-pixel numbers for each wavelength for the chosen wavelength spectrum is found from Eq. (10).

$$x = \frac{-a(y)+\lambda}{b(y)} = -\frac{a(y)}{b(y)} + \frac{\lambda}{b(y)} \tag{10}$$

Thus, *x*-pixels of CMOS image sensor are mapped to the wavelength spectrum as shown in Figure-4.2.

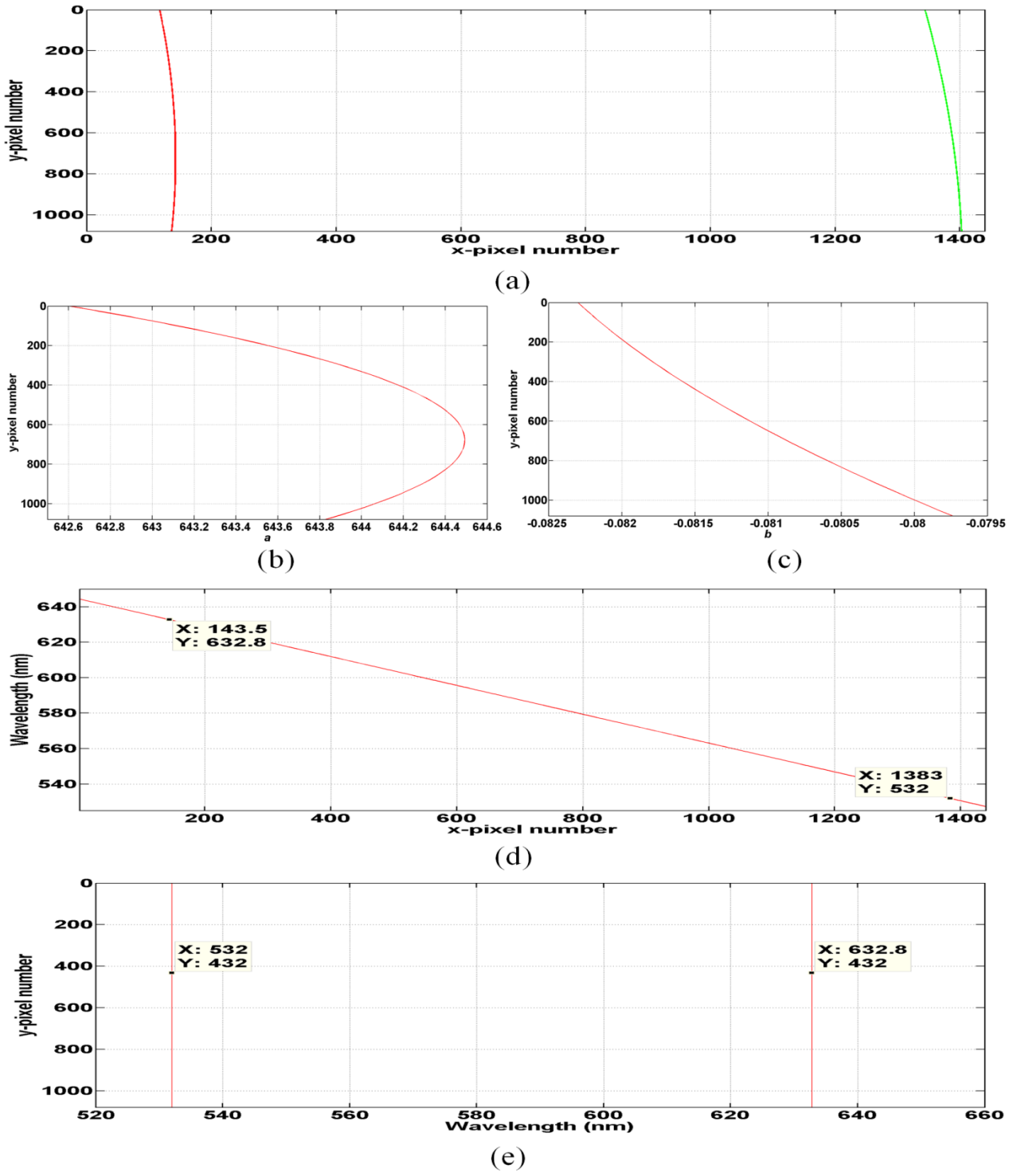

Figure-4.2: Mapping of *x*-pixels of the image sensor to the wavelength spectrum, (a) the pixel locations corresponding to the diffracted images of green and red monochromatic inputs, (b) shows the values of $a(y)$ for entire 1080 *y*-pixels, (c) shows the values of $b(y)$ for entire 1080 *y*-pixels, (d) wavelength versus *x*-pixels showing linear relation, (e) *y*-pixels versus wavelength which is the desired output after mapping. After Chandramohan *et al* Appl. Spectrosc. **70**, 756-765 (© 2016).

Figure-4.2 (a) shows the pixel locations corresponding to the diffracted images of green and red monochromatic inputs as the graphical representation of the intensity distributions shown in Figure-3.2. Second-order curves such as parabolas can be used to approximate these arcs. Nevertheless, some misalignment contributes to the parabolas' vertexes not properly located at the same *y*-pixel number. Implementation of the above-described mapping scheme appropriately rescales each *y*-pixel, which transforms the curved lines shown in Figure-4.2 (a) into the vertical straight lines shown in Figure-4.2 (e). Then the registered intensity is averaged along this transformed vertical line, which is a trivial task.

4.2 Measurement mode

The measurement mode of algorithm is used to display the output of the miniature spectrometer, once the calibration procedure is executed after the initial assembly. The calibrated data is used by measurement mode and the registered light intensity is averaged in real-time to display the output of the miniature spectrometer.

4.3 Averaging phase

Averaging phase is used in both calibration mode and measurement mode of the algorithm. As mentioned earlier, since the light is diverged in the plane of the waveguide, the light hits the entire length of the grating in the waveguide film rather than a single particular location. Therefore, the diffracted images of green and red monochromatic inputs registered on the CMOS image sensor are shaped as arcs and have discontinuous high and low intensities. So selecting a single *y*-pixel from this diffracted image to display the output of the miniature spectrometer will result in discarding most of the registered intensities. Therefore, the averaging needs to be done to collect all the registered intensity along the entire arc. This helps to enhance the sensitivity of the miniature spectrometer. The averaged signal is plotted against the already

mapped wavelength spectrum to display the output of the miniature spectrometer as shown in Figure-4.3.

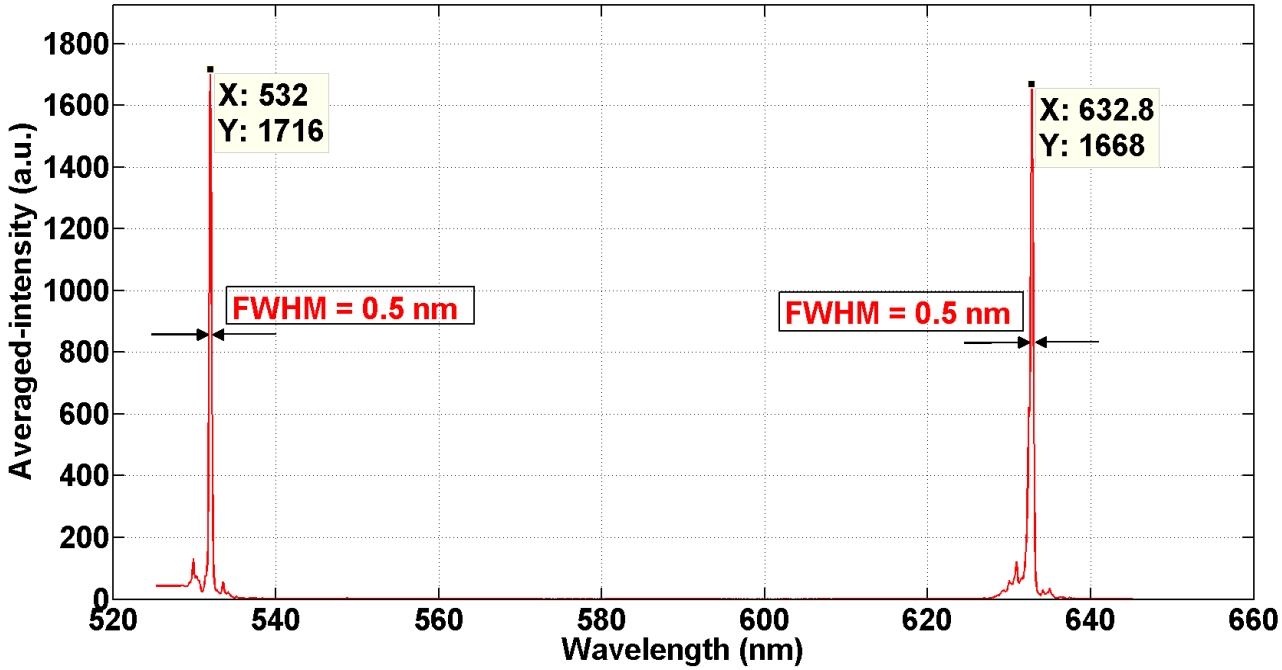

Figure-4.3: Output of miniature spectrometer (Averaged-intensity versus Wavelength) showing spectral resolution of 0.5 nm.

The spectral resolution is given by the full width at half maximum (FWHM). From Figure-4.3, FWHM for both green and red monochromatic inputs are found to be 0.5 nm. This concludes that the resolving power of the miniature spectrometer in a 117 nm wide visible spectrum, from 527.4 nm to 644.4 nm is 0.5 nm. Compared to the conventional desktop spectrometers, this is not a high resolving power but still can be considered a decent value. This indicates a tradeoff that comes at the cost of compact optical design and enhanced sensitivity.

CHAPTER 5: TESTING THE ACCURACY OF THE MAPPING AND SENSITIVITY OF MINIATURE SPECTROMETER

5.1 Testing the accuracy of the mapping scheme using a LED

The mapping scheme implemented in the algorithm is tested for accuracy and reliability. A LED of wavelength 597 nm is used for testing, which falls in between the wavelengths of green (532 nm) and red (632.8 nm) monochromatic inputs in the calibration procedure. First, a conventional spectrometer, Digikrom DK 240 is used to measure the spectrum of LED, which shows the LED peak at 597 nm as shown in Figure-5.1 (a). Then the LED is combined with the green and red monochromatic sources and inputted to the miniature spectrometer to measure the spectrum. The LED peak is found at 597 nm in the output of the miniature spectrometer as shown in Figure-5.1 (b), which is evidently matching with the measurements of the conventional spectrometer. From Figure-5.1 (a) and (b), the spectral resolutions calculated for the spectrums measured by the conventional spectrometer as well as the miniature spectrometer, is found to be 15.1 nm, which is also matching. This confirms the accuracy of the mapping scheme implemented.

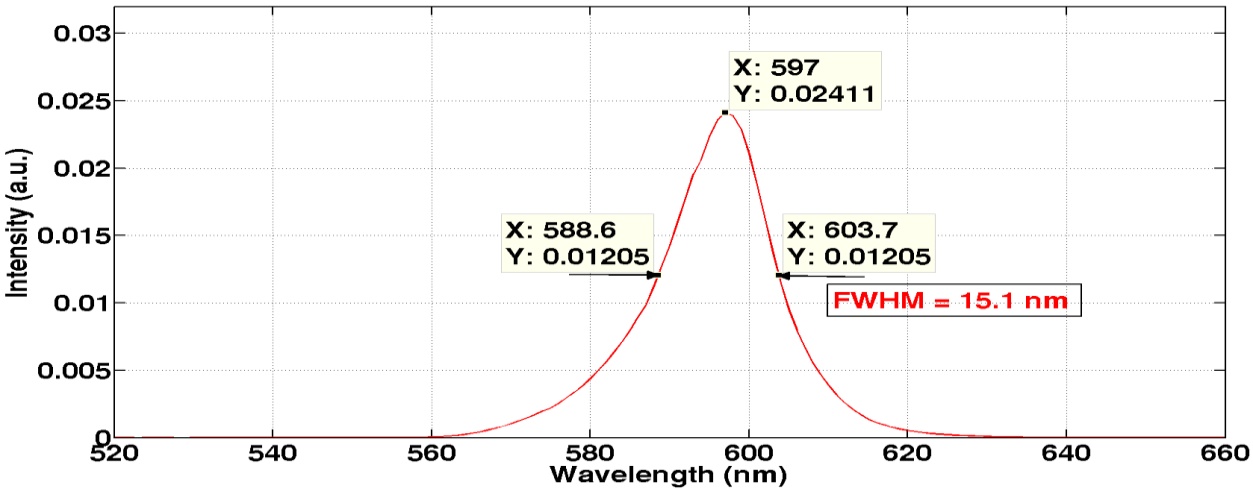

(a)

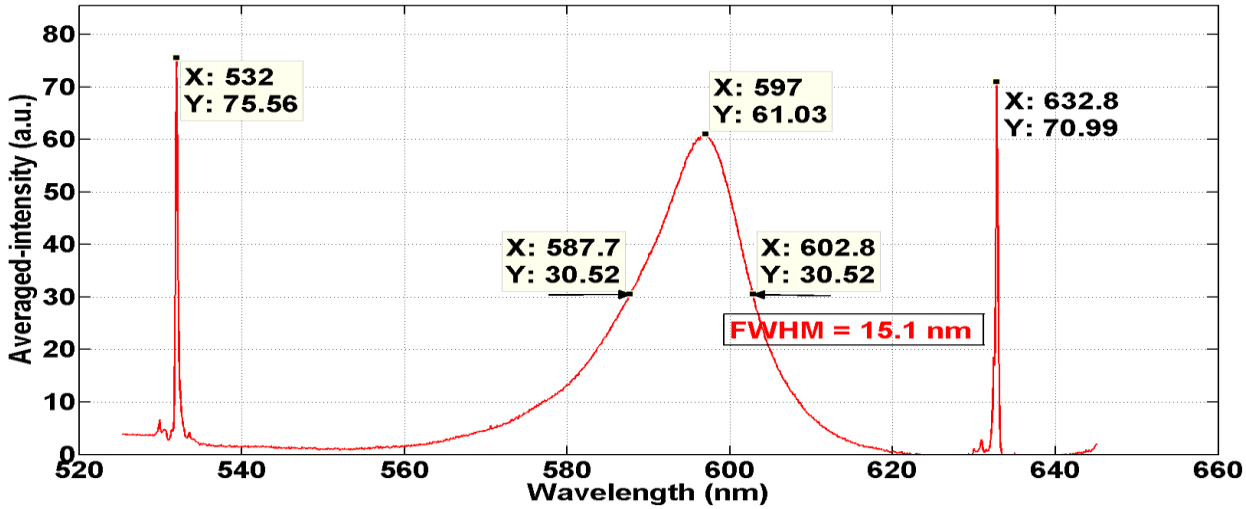

(b)

Figure-5.1: (a) LED spectrum measured by conventional spectrometer (b) LED spectrum measured by miniature spectrometer. After Chandramohan *et al* Appl. Spectrosc. **70**, 756-765 (© 2016).

5.2 Testing the sensitivity of miniature spectrometer

Two different methods are used to test the sensitivity of miniature spectrometer. First method is by lowering the power of green and red monochromatic inputs to 0.1nW using attenuators. In the second method, semiconductor quantum dots are used as test material and quantitative analysis is done to find the number of monolayer of quantum dots participating in the absorption by these quantum dots and predicts the attenuation introduced by a monolayer of these quantum dots, which gives the measure of sensitivity of the device.

5.2.1 Lowering the input power

The sensitivity of the miniature spectrometer is tested in this method by lowering the power of input monochromatic laser sources. The power of each monochromatic input are first measured separately using a power meter, Thorlabs PM100D before the microscope objective. Then the power is lowered to 0.1 nW using attenuators for each monochromatic inputs. To test the sensitivity, the output of miniature spectrometer is displayed by selecting a single *y*-pixel and using the real-time image-processing algorithm as shown in Figure-5.2.

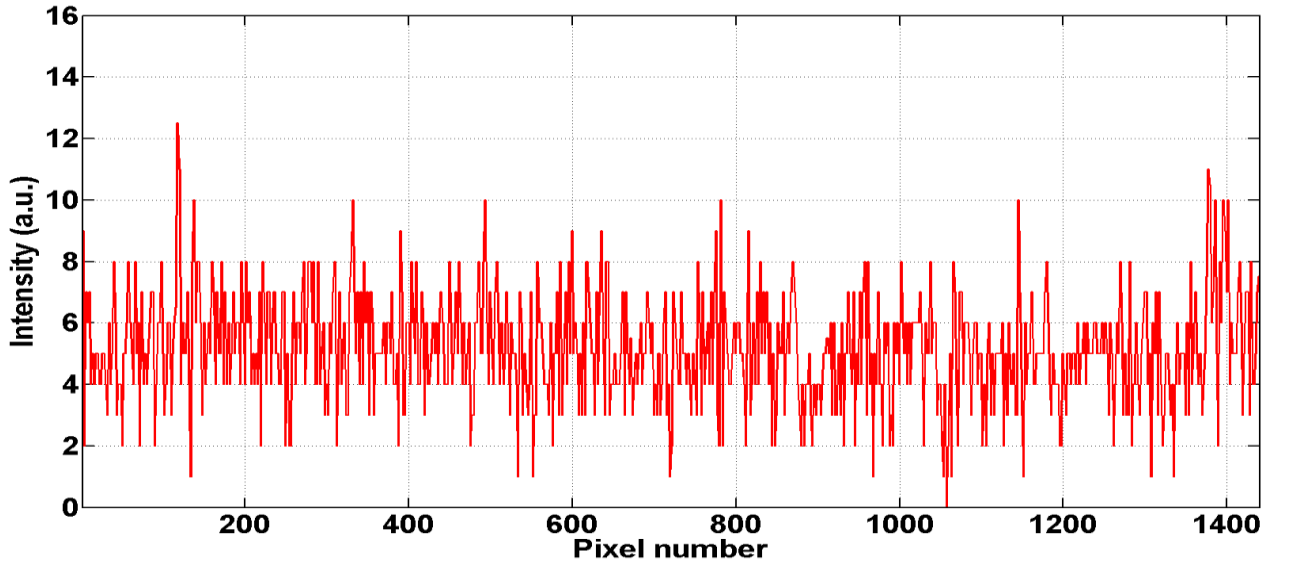

(a)

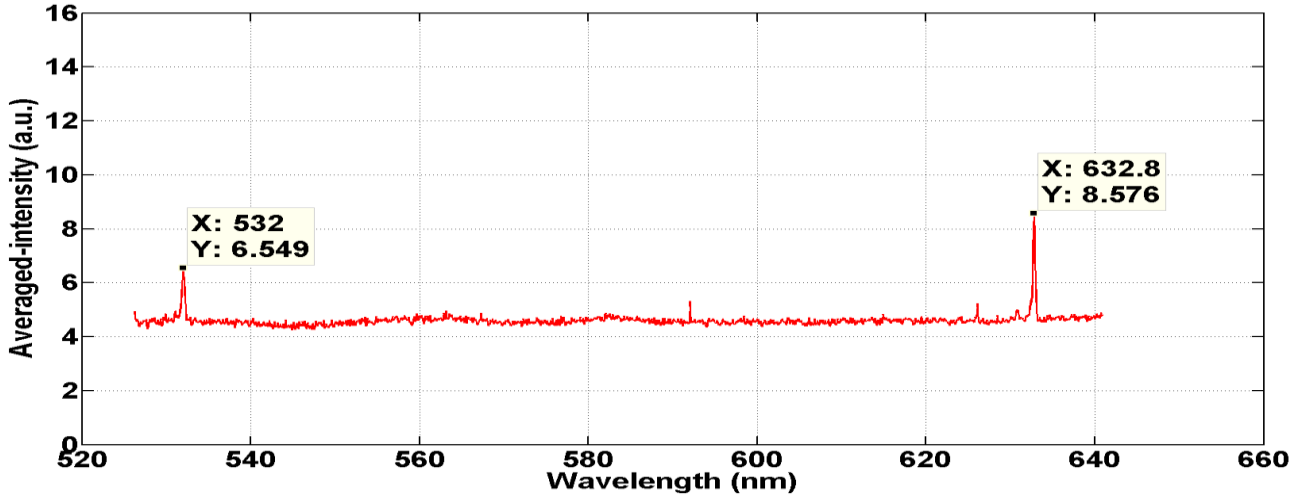

(b)

Figure-5.2: (a) Output of miniature spectrometer for a selected single *y*-pixel for input power of 0.1 nW, (b) Output of miniature spectrometer for input power of 0.1 nW using the real-time image processing algorithm. After Chandramohan *et al* Appl. Spectrosc. **70**, 756-765 (© 2016).

In Figure-5.2 (a), for the selected *y*-pixel, *x*-pixel numbers for the monochromatic inputs 532 nm and 632.8 nm are 155 and 1380 respectively. However, no peaks are observed for *x*-pixel numbers 155 and 1380 due to the noise in the data. However, the peaks of green and red monochromatic inputs are clearly visible well above the noise level in Figure-5.2 (b). This is made possible by the novel approach of averaging along the arcs in the real-time image-processing algorithm. The image-processing algorithm helps to resolve the peaks of green and

red monochromatic inputs above the noise level even at low input power of 0.1 nW. Thus confirming the high sensitivity of the miniature spectrometer.

5.2.2 Using quantum dots

The sensitivity of the miniature spectrometer is tested in this method by drop casting CdSeS/ZnS quantum dots between the gratings of a tantalum pentoxide (Ta_2O_5) planar single-mode waveguide on schott desag D263 substrate, from Optics Balzers [83]. The tantalum pentoxide (Ta_2O_5) waveguide film used here contains two sets of integrated gratings. The refractive index of the tantalum pentoxide (Ta_2O_5) waveguide film is 2.16, and the substrate is 1.5195. The in-coupling and out-coupling gratings have a period of 318 nm. CdSeS/ZnS quantum dots used is a colloidal solution diluted in toluene from Cytodiagnostics [84], which can be pumped using wavelength of 532 nm and emits at a wavelength of 575±5 nm. The diameter of the drop casted quantum dots is made to be 0.7 mm. The experimental setup to test the sensitivity is shown in Figure-5.3.

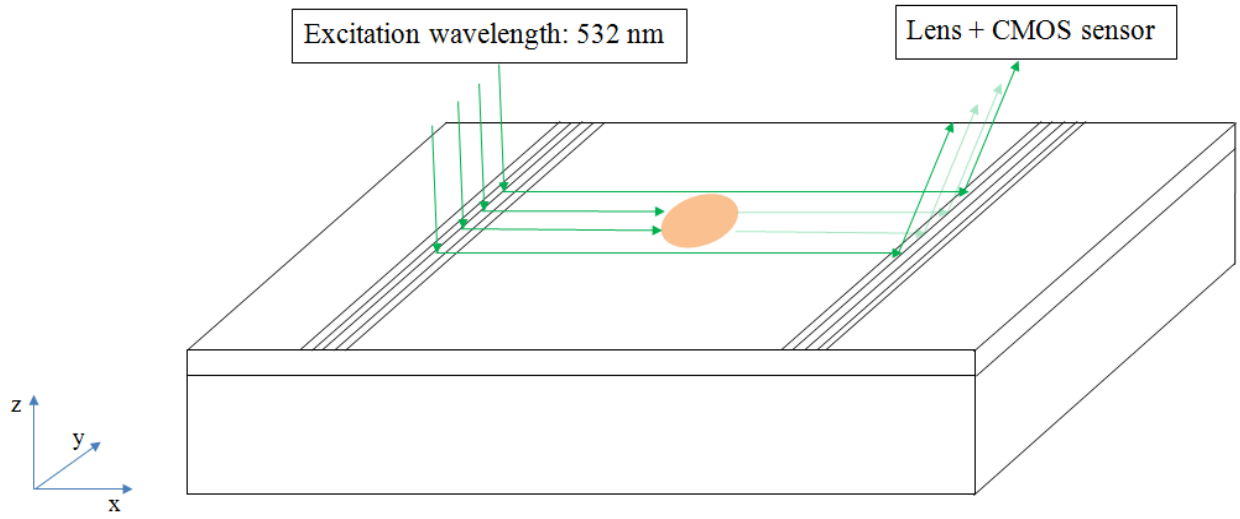

Figure-5.3: Experimental setup for testing the sensitivity using quantum dots. After Chandramohan *et al* Appl. Spectrosc. **70**, 756-765 (© 2016).

The experimental procedure for testing the sensitivity is as follows. The green laser beam is moved in 0.1 mm succession along the entire length of in-coupling grating in *y*-axis direction.

The beam moves through the drop casted 0.7 mm diameter quantum dots. The spectrum is measured for the whole procedure and the registered intensities are compared with and without the presence of quantum dots. This quantitatively measures the degree of absorption introduced by drop casted quantum dots.

Assuming the quantum dots are stacked as monolayer while drop casting, the number of monolayer of quantum dots participating in the absorption is determined. To determine the number of monolayer of quantum dots participating in the absorption, the effective index of refraction for TE_0 component of electric field (fundamental TE component) is needed to be determined first using the known refractive indices for film, n_f =2.16, substrate, n_s = 1.5195 and cover, n_c = 1.5019 (which is the drop casted quantum dots) [85]. From Figure-5.4, the effective index of refraction for TE_0 component of electric field for the excitation wavelength of 532 nm is found to be 1.902.

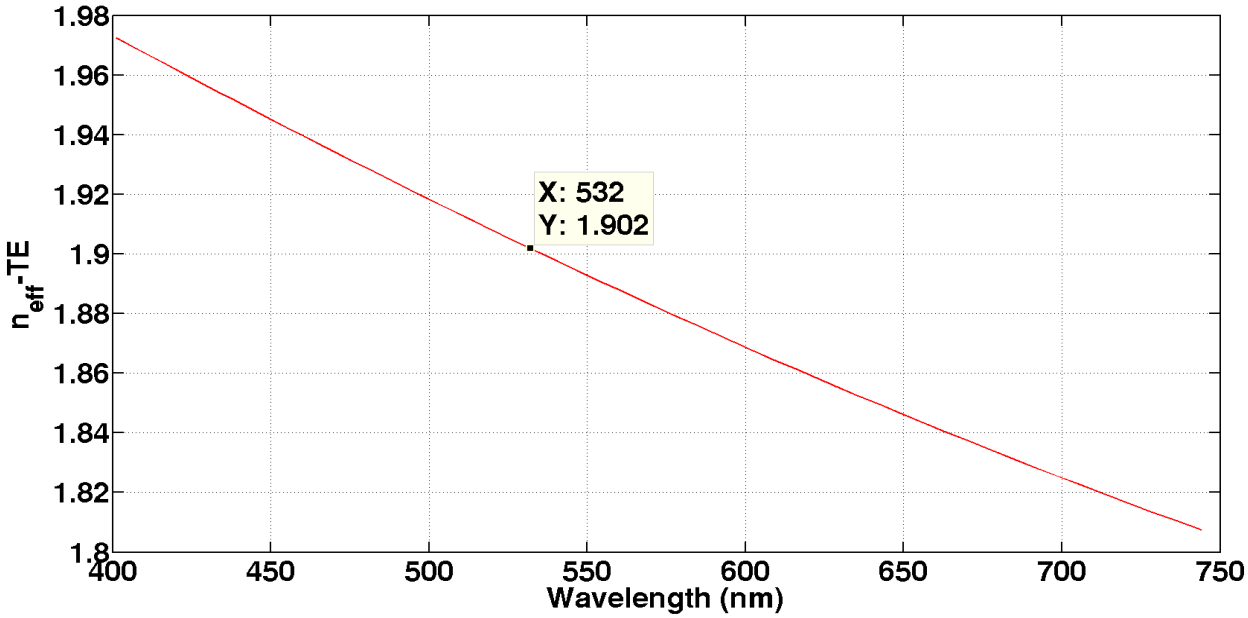

Figure-5.4: Effective index for TE_0 component of electric field.

The next step is to find the penetration depth of evanescent field of the electric field from the equation of electric field given by $|E|^2 = |E_0|^2 e^{-2qy}$. Here $q = \frac{2\pi}{\lambda}\sqrt{n_{eff}^{\ 2} - n_c^{\ 2}}$ is the attenuation factor of evanescent field. The penetration depth of the evanescent field is then calculated from the attenuation factor, given by Eq. (11).

$$d_{|E|^2} = \frac{1}{2q} = \frac{\lambda}{4\pi\sqrt{n_{eff}^{\ 2} - n_c^{\ 2}}} \tag{11}$$

The electric field equation mentioned above is then plotted to verify the penetration depth of the evanescent field calculated using Eq. (11) as shown in Figure-5.5 and is found to be 36.2 nm.

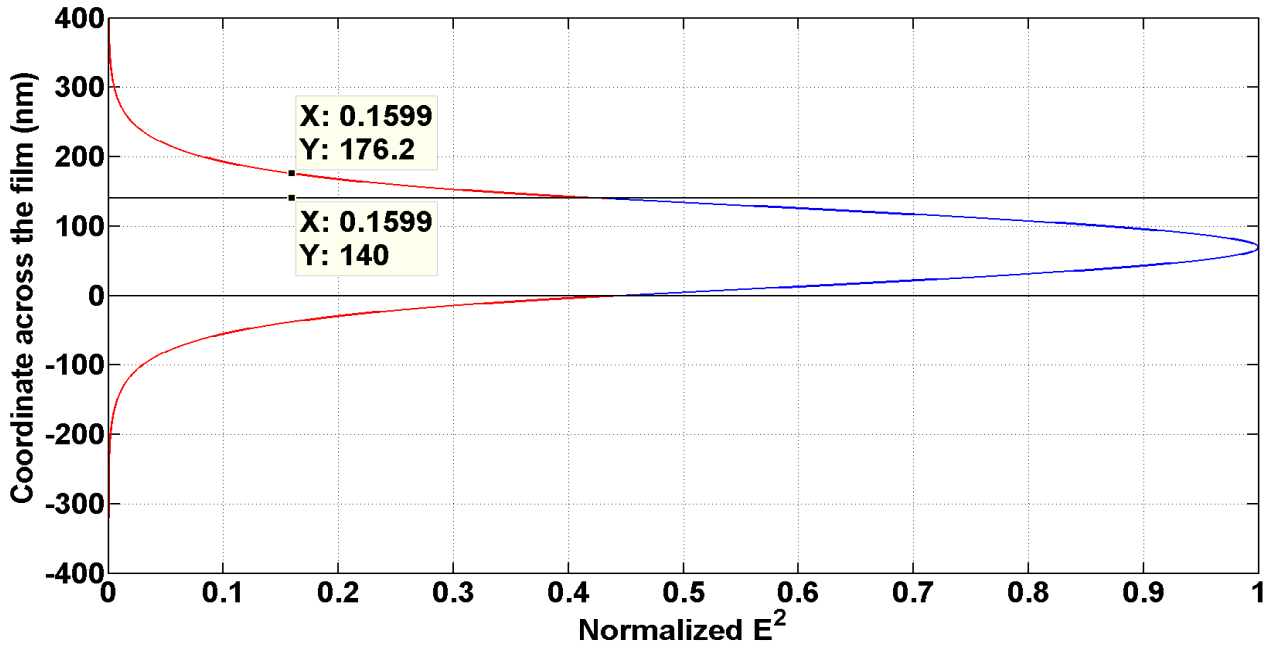

Figure-5.5: Evanescent field of electric field showing penetration depth of 36.2 nm.

Absorption measurement to test the sensitivity of the miniature spectrometer is achieved using the experimental setup shown in Figure-5.3 and the result obtained is shown in Figure-5.6. From Figure-5.6, the average intensities for regions without quantum dot absorption is found to be I_0=3326.

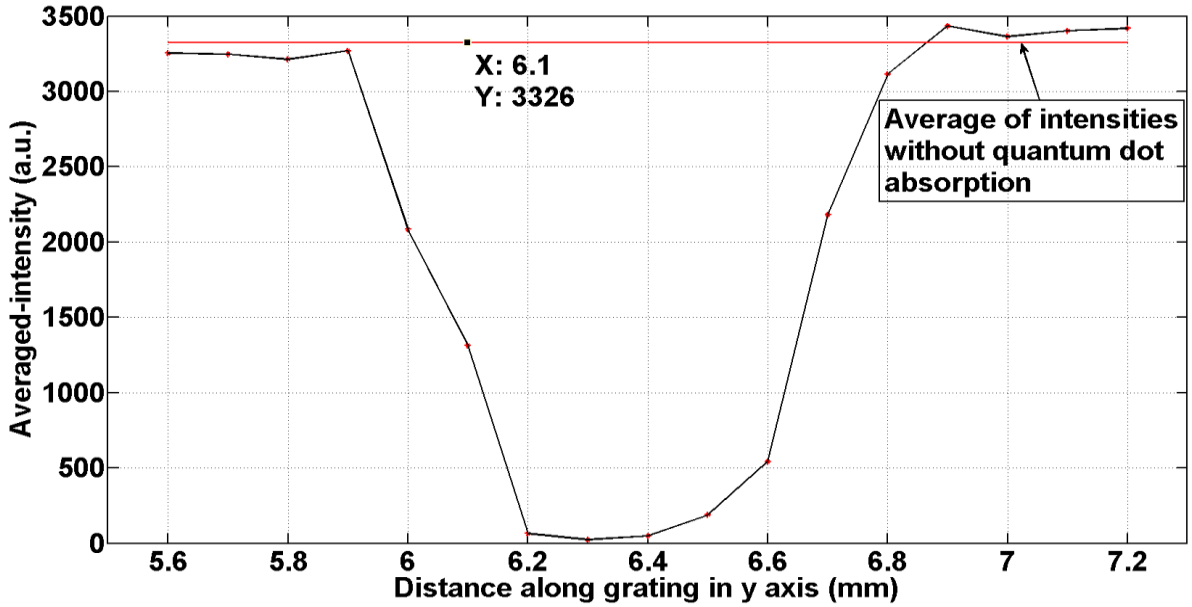

Figure-5.6: Absorption measured by miniature spectrometer. After Chandramohan *et al* Appl. Spectrosc. **70**, 756-765 (© 2016).

The attenuation factor is then calculated using the equation given in Eq. (12) and the result is shown in Figure-5.7.

$$\alpha = -\frac{1}{D}\ln\left(\frac{I}{I_0}\right) \tag{12}$$

Here, D is the diameter of the drop casted quantum dots, I is the intensity measured by the miniature spectrometer and I_0 is the average intensities for regions without quantum dots.

From Figure-5.7, the attenuation due to absorption by the quantum dots for three measured points in the middle of the drop casted quantum dots is found to be 62.4 cm^{-1}. Since the size of a single quantum dot is six nm, the penetration depth of evanescent field found from Figure-5.5 gives the number of monolayer of quantum dots participating in the absorption, which is 36.2 / 6 = 6 monolayer of quantum dots approximately. Thus, the average attenuation level of 62.4 cm^{-1} found for the three measured points in the middle of the drop casted quantum dots indicates the absorption by six layers of quantum dots. Then the attenuation expected to be

produced by monolayer of quantum dots is calculated as 62.4 / 6 = 10.4 cm^{-1}. Since the highest noise level found from Figure-5.7 is 0.9398 cm^{-1}, the attenuation produced by monolayer of quantum dots is approximately10.4 / 0.9398=11 times above this noise level.

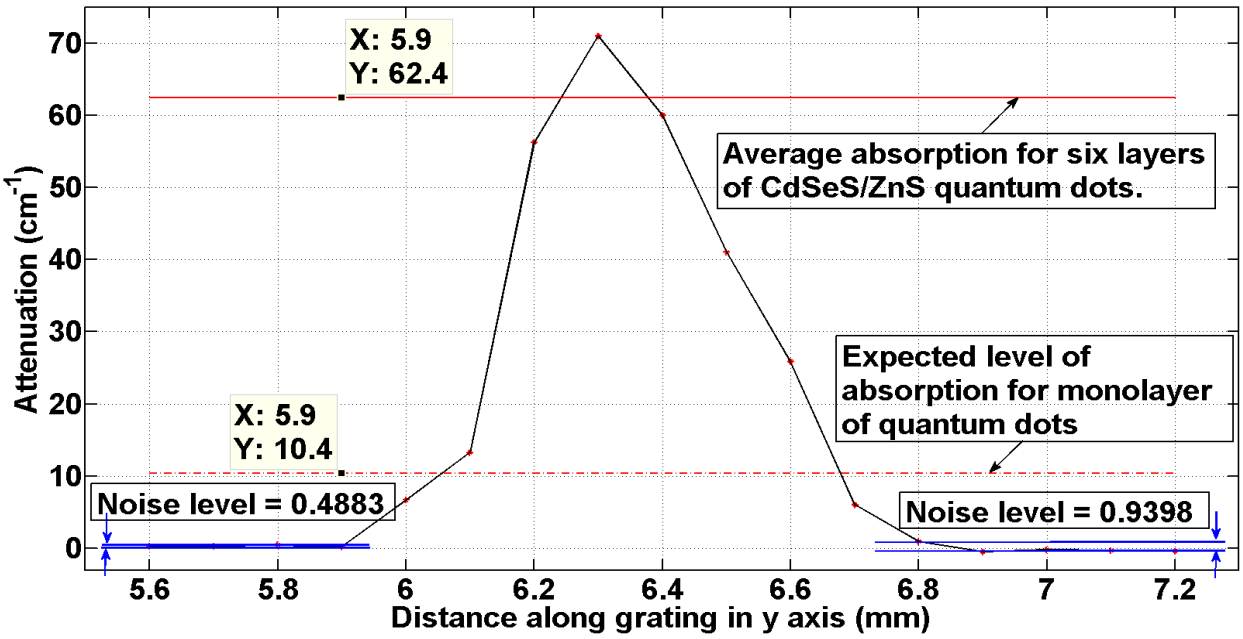

Figure-5.7: Attenuation calculated from the absorption measured by miniature spectrometer. After Chandramohan *et al* Appl. Spectrosc. **70**, 756-765 (© 2016).

5.3 Comparison of sensitivity with known devices

The measure of sensitivity i.e. detection limit of biosensors and chemical sensors reported in [56-62] is based on the minimum refractive index change that can be measured using the device in refractive index units. Since the miniature spectrometer in this study is a direct spectroscopic absorption sensor based on ATR, the sensitivity comparison with ATR spectrometers for thin film characterization is done with the detection limit as the detection of minimum film thickness possible with these devices. Mendes *et al* [86] reported planar waveguide attenuated total reflectance (ATR) spectrometer with spectral resolution of 0.7 nm and characterization of molecular monolayer of protein of thickness approximately 3 nm. Mukundan *et al* [59] reported a waveguide-based biosensor with biological detection target (50

kDa protein) of approximately 5 nm in size. The monolayer of quantum dots used for sensitivity analysis in miniature spectrometer can be assumed as 6 nm thin layer on the surface of the waveguide. The attenuation of evanescent field by this 6 nm thin layer is found to be 11 times above the noise level of the system. Hence, the miniature spectrometer will be capable of measuring the monolayer of thickness 3 nm. Thus, the sensitivity of this device is comparable to the devices reported in [59, 86].

CHAPTER 6: CONCLUSION

For the fabrication, investigation of focused ion beam (FIB) parameters for the successful fabrication of sub-micrometer dense patterns on hard transition metal nitride such as zirconium nitride (ZrN) is demonstrated. Appropriate values for ion beam current, magnification, dwell time, milling rate etc are investigated. Gratings are used as dense pattern on ZrN. The milled patterns are characterized using scanning electron microscope (SEM) and atomic force microscope (AFM).

The actual milling rate is found by fabricating gratings with period of 540 nm and depth of grooves, 50 nm. The gratings are fabricated with different dwell times for already known milling rates of common materials in the manufacturer software as well as manually setting some milling rates. These set manual milling rates are used to calculate the time of exposure of ion beam for milling the gratings. These values of calculated time of exposure are then used to calculate the ion dose involved in the milling process. The ion dose thus calculated along with the milled depth obtained from AFM for these fabricated gratings are used to find the actual milling rate.

Concluding, the appropriate FIB parameters for pattern of dimension 500 nm on ZrN are as follows. The ion beam current is found to be 50 pA or less. The magnification is 2 kx. The actual milling rate is found to be 0.076 $\mu m^3/ (nA \cdot s)$ for dwell time of 1 µs and 0.07 $\mu m^3/ (nA \cdot s)$ for dwell times of 5 µs, 10 µs and 15 µs.

For device performance, a real-time image-processing algorithm is developed to enhance the sensitivity of an optical miniature spectrometer. The novel approach in this design is the use of real-time image processing algorithm to average the image intensity along the arc shaped images registered by the monochromatic inputs on the CMOS image sensor, which helps to

collect the light from the entire arc and thus enhancing the sensitivity of the device. The algorithm is developed using $SiTiO_2$ planar waveguide on a BK7 substrate. The accuracy of the mapping from *x*-pixel number scale of the CMOS image sensor to the wavelength spectra is demonstrated by measuring the spectrum of an LED with wavelength of 597 nm, (which falls in between the green and red laser beam wavelengths) using a conventional desktop spectrometer and compared it with the spectrum measured by the miniature spectrometer.

The sensitivity of miniature spectrometer is demonstrated by attenuating the laser power to 0.1 nW as well as doing a quantitative analysis by measuring the absorption of CdSeS/ZnS quantum dots drop casted between the gratings of Ta_2O_5 planar single-mode waveguide on a Schott Desag D263 substrate. The absorption is measured along the y-axis direction of the grating. The number of layers of quantum dots participating in the absorption measured is determined and found to be approximately six layers of quantum dots. These six layers of quantum dots produce an average attenuation of 62.4 cm^{-1} for three measured points in the middle of the drop casting. Thus, estimated attenuation for monolayer of quantum dots can be found from the absorption by six layers, which is 10.4 cm^{-1}. This value is approximately 11 times higher than the highest noise level of 0.9398 cm^{-1}.

APPENDIX: LIST OF PUBLICATIONS

- Sabarish Chandramohan, and Ivan Avrutsky. "Enhancing Sensitivity of a Miniature Spectrometer Using a Real-Time Image Processing Algorithm." *Applied spectroscopy* 70, no. 5 (2016): 756-765.
- Sabarish Chandramohan. "Real-Time High Resolution Integrated Optical Micro-Spectrometer." (2014).

REFERENCES

[1] Chung-Soo Kim, Sung-Hoon Ahn, and Dong-Young Jang. "Review: Developments in micro/nanoscale fabrication by focused ion beams." *Vacuum* 86, no. 8 (2012): 1014-1035.

[2] Ampere A Tseng. "Recent developments in micromilling using focused ion beam technology." *Journal of Micromechanics and Microengineering* 14, no. 4 (2004): R15.

[3] David J. Moss, Vahid G. Ta'eed, Benjamin J. Eggleton, Darren Freeman, Steve Madden, Marek Samoc, Barry Luther-Davies, Siegfried Janz, and D-X. Xu. "Bragg gratings in silicon-on-insulator waveguides by focused ion beam milling." *Applied physics letters* 85, no. 21 (2004): 4860-4862.

[4] Yanxin Liu, Chao Meng, A. Ping Zhang, Yao Xiao, Huakang Yu, and Limin Tong. "Compact microfiber Bragg gratings with high-index contrast." *Optics letters* 36, no. 16 (2011): 3115-3117.

[5] Ji Cheng, and A. J. Steckl. "Focused ion beam fabricated microgratings for integrated optics applications." *Selected Topics in Quantum Electronics, IEEE Journal of* 8, no. 6 (2002): 1323-1330.

[6] Yongqi Fu, Ngoi Kok Ann Bryan, and Ong Nan Shing. "Microfabrication of diffractive optical element with continuous relief by focused ion beam." *Microelectronic engineering* 54, no. 3 (2000): 287-293.

[7] C. Aubry, T. Trigaud, J. P. Moliton, and D. Chiron. "Polymer gratings achieved by focused ion beam." *Synthetic metals* 127, no. 1 (2002): 307-311.

[8] Wuxia Li, Georgi Lalev, Stefan Dimov, Hao Zhao, and D. T. Pham. "A study of fused silica micro/nano patterning by focused-ion-beam." *Applied surface science* 253, no. 7 (2007): 3608-3614.

[9] Wico CL Hopman, Feridun Ay, Wenbin Hu, Vishwas J. Gadgil, Laurens Kuipers, Markus Pollnau, and René M. de Ridder. "Focused ion beam scan routine, dwell time and dose optimizations for submicrometre period planar photonic crystal components and stamps in silicon." *Nanotechnology* 18, no. 19 (2007): 195305.

[10] Kalyani Chaganti, Ildar Salakhutdinov, Ivan Avrutsky, Gregory Auner, and John Mansfield. "Sub-micron grating fabrication on hafnium oxide thin-film waveguides with focused ion-beam milling." *Optics express* 14, no. 4 (2006): 1505-1511.

[11] Kirill Zinoviev, Carlos Dominguez, and Anna Vilà. "Diffraction grating couplers milled in Si3N4 rib waveguides with a focused ion beam." *Optics express* 13, no. 21 (2005): 8618-8624.

[12] S.Cabrini, L. Businaro, M. Prasciolu, A. Carpentiro, D. Gerace, M. Galli, L. C. Andreani, F. Riboli, L. Pavesi, and E. Di Fabrizio. "Focused ion beam fabrication of one-dimensional photonic crystals on Si3N4/SiO2 channel waveguides." *Journal of Optics A: Pure and Applied Optics* 8, no. 7 (2006): S550.

[13] Ruby Dela Torre, Joseph Larkin, Alon Singer, and Amit Meller. "Fabrication and characterization of solid-state nanopore arrays for high-throughput DNA sequencing." *Nanotechnology* 23, no. 38 (2012): 385308.

[14] V. J. Gadgil, H. D. Tong, Y. Cesa, and M. L. Bennink. "Fabrication of nano structures in thin membranes with focused ion beam technology." *Surface and Coatings Technology* 203, no. 17 (2009): 2436-2441.

[15] Yvonne H. Lanyon, Gianluca De Marzi, Yvonne E. Watson, Aidan J. Quinn, James P. Gleeson, Gareth Redmond, and Damien WM Arrigan. "Fabrication of nanopore array electrodes by focused ion beam milling." *Analytical chemistry* 79, no. 8 (2007): 3048-3055.

[16] Hien D. Tong, Henri V. Jansen, Vishwas J. Gadgil, Cazimir G. Bostan, Erwin Berenschot, Cees JM van Rijn, and Miko Elwenspoek. "Silicon nitride nanosieve membrane." *Nano letters* 4, no. 2 (2004): 283-287.

[17] Shuanglin Yue, and Changzhi Gu. "Nanopores fabricated by focused ion beam milling technology." Proceedings of the *7th IEEE Conference on Nanotechnology (IEEE NANO)*, (2007): pp. 628-631.

[18] A. J. Steckl, and I. Chyr. "Focused ion beam micromilling of GaN and related substrate materials (sapphire, SiC, and Si)." *Journal of Vacuum Science & Technology B* 17, no. 2 (1999): 362-365.

[19] Qian Ren, Bei Zhang, Jun Xu, YanBo Jin, ZhiJian Yang, XiaoDong Hu, ZhiXin Qin, ZhiZhong Chen, XiaoMin Ding, YuZhen Tong, ZhenSheng Zhang, GuoYi Zhang, DaPeng Yu, and ZiZhao Gan. "The fabrication of GaN-based optical cavity mirrors by focused ion beam milling." *physica status solidi (c)* 7 (2003): 2300-2303.

[20] Bei Zhang, ZhenSheng Zhang, Jun Xu, Qian Ren, ChunLai Jin, ZhiJian Yang, Qi Wang, WeiHua Chen, XiaoDong Hu, TongJun Yu, ZhiXin Qin, GuoYi Zhang, DaPeng Yu, and BaoPing Zhang. "Effects of the artificial Ga-nitride/air periodic nanostructures on current injected GaN-based light emitters." *physica status solidi (c)* 2, no. 7 (2005): 2858-2861.

[21] Gururaj V. Naik, Vladimir M. Shalaev, and Alexandra Boltasseva. "Alternative plasmonic materials: beyond gold and silver." *Advanced Materials* 25, no. 24 (2013): 3264-3294.

[22] Urcan Guler, Vladimir M. Shalaev, and Alexandra Boltasseva. "Nanoparticle plasmonics: going practical with transition metal nitrides." *Materials Today* 18, no. 4 (2015): 227-237.

[23] Urcan Guler, Alexandra Boltasseva, and Vladimir M. Shalaev. "Refractory plasmonics." *Science* 344, no. 6181 (2014): 263-264.

[24] Gururaj V. Naik, Jongbum Kim, and Alexandra Boltasseva. "Oxides and nitrides as alternative plasmonic materials in the optical range [Invited]." *Optical Materials Express* 1, no. 6 (2011): 1090-1099.

[25] Gururaj V. Naik, Bivas Saha, Jing Liu, Sammy M. Saber, Eric A. Stach, Joseph MK Irudayaraj, Timothy D. Sands, Vladimir M. Shalaev, and Alexandra Boltasseva. "Epitaxial super lattices with titanium nitride as a plasmonic component for optical hyperbolic metamaterials." *Proceedings of the National Academy of Sciences* 111, no. 21 (2014): 7546-7551.

[26] Mikhail Y. Shalaginov, Vadim V. Vorobyov, Jing Liu, Marcello Ferrera, Alexey V. Akimov, Alexei Lagutchev, and Andrey N. Smolyaninov. "Enhancement of single-photon emission from nitrogen-vacancy centers with TiN/(Al, Sc) N hyperbolic metamaterial." *Laser & Photonics Reviews* 9, no. 1 (2015): 120-127.

[27] Nathaniel Kinsey, Marcello Ferrera, Gururaj V. Naik, V. E. Babicheva, Vladimir M. Shalaev, and Alexandra Boltasseva. "Experimental demonstration of titanium nitride plasmonic interconnects." *Optics express* 22, no. 10 (2014): 12238-12247.

[28] Urcan Guler, Justus C. Ndukaife, Gururaj V. Naik, AG Agwu Nnanna, Alexander V. Kildishev, Vladimir M. Shalaev, and Alexandra Boltasseva. "Local heating with lithographically fabricated plasmonic titanium nitride nanoparticles." *Nano letters* 13, no. 12 (2013): 6078-6083.

[29] Wei Li, Urcan Guler, Nathaniel Kinsey, Gururaj V. Naik, Alexandra Boltasseva, Jianguo Guan, Vladimir M. Shalaev, and Alexander V. Kildishev. "Refractory plasmonics with titanium nitride: broadband metamaterial absorber." *Advanced Materials* 26, no. 47 (2014): 7959-7965.

[30] Jingjing Liu, Urcan Guler, Alexei Lagutchev, Alexander Kildishev, Oana Malis, Alexandra Boltasseva, and Vladimir M. Shalaev. "Quasi-coherent thermal emitter based on refractory plasmonic materials." *Optical Materials Express* 5, no. 12 (2015): 2721-2728.

[31] Urcan Guler, Sergey Suslov, Alexander V. Kildishev, Alexandra Boltasseva, and Vladimir M. Shalaev. "Colloidal plasmonic titanium nitride nanoparticles: properties and applications." *Nanophotonics* 4, no. 1 (2015).

[32] Kalyani Chaganti, Ildar Salakhutdinov, Ivan Avrutsky, and Gregory W. Auner. "A simple miniature optical spectrometer with a planar waveguide grating coupler in combination with a plano-convex lens." *Optics Express* 14, no. 9 (2006): 4064-4072.

[33] Ivan Avrutsky, Kalyani Chaganti, Ildar Salakhutdinov, and Gregory Auner. "Optical micro-spectrometer with sub-nanometer resolution." In *NSTI-Nanotech*, vol. 3, pp. 328-331. 2006.

[34] Semen Grabarnik, Arvin Emadi, Huaiwen Wu, Ger De Graaf, and Reinoud F. Wolffenbuttel. "High-resolution microspectrometer with an aberration-correcting planar grating." *Applied optics* 47, no. 34 (2008): 6442-6447.

[35] Ivan Avrutsky, Kalyani Chaganti, Ildar Salakhutdinov, and Gregory Auner. "Concept of a miniature optical spectrometer using integrated optical and micro-optical components." *Applied optics* 45, no. 30 (2006): 7811-7817.

[36] Robert Brunner, Matthias Burkhardt, Klaus Rudolf, and Nico Correns. "Microspectrometer based on holographically recorded diffractive elements using supplementary holograms." *Optics express* 16, no. 16 (2008): 12239-12250.

[37] Semen Grabarnik, Reinoud Wolffenbuttel, Arwin Emadi, Mikhail Loktev, Elena Sokolova, and Gleb Vdovin. "Planar double-grating microspectrometer." *Optics express* 15, no. 6 (2007): 3581-3588.

[38] Semen Grabarnik, Arvin Emadi, Elena Sokolova, Gleb Vdovin, and Reinoud F. Wolffenbu-ttel. "Optimal implementation of a microspectrometer based on a single flat diffraction grating." *Applied optics* 47, no. 12 (2008): 2082-2090.

[39] Shogo Ura, Fumikazu Okayama, Koichi Shiroshita, Kenzo Nishio, Takahiro Sasaki, Hiroshi Nishihara, Tsutom Yotsuya, Masato Okano, and Kazuo Satoh. "Planar reflection grating lens for compact spectroscopic imaging system." *Applied optics* 42, no. 2 (2003): 175-180.

[40] Dietmar Sander, Oliver Blume, and Jörg Müller. "Microspectrometer with slab-waveguide transmission gratings." *Applied optics* 35, no. 21 (1996): 4096-4101.

[41] Chuan Yang, Perry Edwards, Kebin Shi, and Zhiwen Liu. "Proposal and demonstration of a spectrometer using a diffractive optical element with dual dispersion and focusing functionality." *Optics letters* 36, no. 11 (2011): 2023-2025.

[42] Shao-Wei Wang, Changsheng Xia, Xiaoshuang Chen, Wei Lu, Ming Li, Haiqian Wang, Weibo Zheng, and Tao Zhang. "Concept of a high-resolution miniature spectrometer using an integrated filter array." *Optics letters* 32, no. 6 (2007): 632-634.

[43] Miroslaw Florjanczyk, Pavel Cheben, Siegfried Janz, Alan Scott, Brian Solheim, and Dan-Xia Xu. "Multiaperture planar waveguide spectrometer formed by arrayed Mach-Zehnder interferometers." *Optics express* 15, no. 26 (2007): 18176-18189.

[44] Gaël Latour, Julien Moreau, Mady Elias, and Jean-Marc Frigerio. "Micro-spectrometry in the visible range with full-field optical coherence tomography for single absorbing layers." *Optics Communications* 283, no. 23 (2010): 4810-4815.

[45] Babak Momeni, Ehsan Shah Hosseini, and Ali Adibi. "Planar photonic crystal microspectrometers in silicon-nitride for the visible range." *Optics express* 17, no. 19 (2009): 17060-17069.

[46] José Higino Correia, Marian Bartek, and Reinoud F. Wolffenbuttel, "High-selectivity single-chip spectrometer in silicon for operation in visible part of the spectrum", IEEE Transactions on Electron Devices, Vol.47, Issue 3, 553 - 559 (2000).

[47] Peng Wang, and Rajesh Menon. "Computational spectrometer based on a broadband diffractive optic." *Optics express* 22, no. 12 (2014): 14575-14587.

[48] R. G. DeCorby, N. Ponnampalam, E. Epp, T. Allen, and J. N. McMullin. "Chip-scale spectrometry based on tapered hollow Bragg waveguides." *Optics express* 17, no. 19 (2009): 16632-16645.

[49] Reinoud F. Wolffenbuttel. "MEMS-based optical mini-and microspectrometers for the visible and infrared spectral range." *Journal of Micromechanics and Microengineering* 15, no. 7 (2005): S145.

[50] Reinoud F. Wolffenbuttel. "State-of-the-art in integrated optical microspectrometers." *IEEE Transactions on Instrumentation and Measurement* 53, no. 1 (2004): 197-202.

[51] Semen Grabarnik, Arvin Emadi, Huaiwen Wu, Ger de Graaf, and Reinoud F. Wolffenbuttel. "Microspectrometer with a concave grating fabricated in a MEMS technology." *Procedia Chemistry* 1, no. 1 (2009): 401-404.

[52] Omar Manzardo, Hans Peter Herzig, Cornel R. Marxer, and Nico F. de Rooij. "Miniaturized time-scanning Fourier transform spectrometer based on silicon technology." *Optics letters* 24, no. 23 (1999): 1705-1707.

[53] Vladislav Jovanov, Jordan Ivanchev, and Dietmar Knipp. "Standing wave spectrometer." *optics express* 18, no. 2 (2010): 426-438.

[54] Christina P. Bacon, Yvette Mattley, and Ronald DeFrece. "Miniature spectroscopic instrumentation: applications to biology and chemistry." *Review of Scientific instruments* 75,

[55] Gaylin M. Yee, Nadim I. Maluf, Paul A. Hing, Michael Albin, and Gregory TA Kovacs. "Miniature spectrometers for biochemical analysis." In *BiOS'97, Part of Photonics West*, pp. 75-81. International Society for Optics and Photonics, 1997.

[56] Xudong Fan, Ian M. White, Siyka I. Shopova, Hongying Zhu, Jonathan D. Suter, and Yuze Sun. "Sensitive optical biosensors for unlabeled targets: A review." *analytica chimica acta* 620, no. 1 (2008): 8-26.

[57] Hikmat N. Daghestani, and Billy W. Day. "Theory and applications of surface plasmon resonance, resonant mirror, resonant waveguide grating, and dual polarization interferometry biosensors." *Sensors* 10, no. 11 (2010): 9630-9646.

[58] Angela Leung, P. Mohana Shankar, and Raj Mutharasan. "A review of fiber-optic biosensors." *Sensors and Actuators B: Chemical* 125, no. 2 (2007): 688-703.

[59] Harshini Mukundan, Aaron S. Anderson, W. Kevin Grace, Karen M. Grace, Nile Hartman, Jennifer S. Martinez, and Basil I. Swanson. "Waveguide-based biosensors for pathogen detection." *Sensors* 9, no. 7 (2009): 5783-5809.

[60] Vittorio Passaro, Francesco Dell'Olio, Biagio Casamassima, and Francesco De Leonardis. "Guided-wave optical biosensors." *Sensors* 7, no. 4 (2007): 508-536.

[61] Colette McDonagh, Conor S. Burke, and Brian D. MacCraith. "Optical chemical sensors." *Chemical reviews* 108, no. 2 (2008): 400-422.

[62] Paul V Lambeck. "Integrated optical sensors for the chemical domain." *Measurement science and technology* 17, no. 8 (2006): R93.

[63] John Thomas Bradshaw, Sergio B. Mendes, and S. Scott Saavedra. "Planar integrated optical waveguide spectroscopy." *Analytical Chemistry* 77, no. 1 (2005): 28-A.

[64] Arvin Emadi, Huaiwen Wu, Ger de Graaf, and Reinoud Wolffenbuttel. "Design and implementation of a sub-nm resolution microspectrometer based on a Linear-Variable Optical Filter." *Optics express* 20, no. 1 (2012): 489-507.

[65] Michal P. Wisniewski, and Roman Z. Morawski. "Algorithms for interpretation of spectrometric data-A comparative study." In *Instrumentation and Measurement Technology Conference, 2000. IMTC 2000. Proceedings of the 17th IEEE,* vol. 2, pp. 703-706. IEEE, 2000.

[66] Daniel Massicotte, Roman Z. Morawski, and Andrzej Barwicz. "Kalman-filter-based algorithms of spectrometric data correction-Part I: an iterative algorithm of deconvolution." *IEEE transactions on instrumentation and measurement* 46, no. 3 (1997): 678-684.

[67] Andrzej Miekina, Roman Z. Morawski, and Andrzej Barwicz. "The use of deconvolution and iterative optimization for spectrogram interpretation." *IEEE transactions on instrumentation and measurement* 46, no. 4 (1997): 1049-1053.

[68] Roman Z. Morawski, and Andrzej Miekina. "Improving absorbance spectrum reconstruction via spectral data decomposition and pseudo-baseline optimization." *IEEE Transactions on Instrumentation and Measurement* 58, no. 3 (2009): 691-697.

[69] Andrzej Miekina, and Roman Z. Morawski. "An Improved Criterion for Inverse-Model-Based Calibration of Spectrophotometric Transducers." In *2007 IEEE Instrumentation & Measurement Technology Conference IMTC 2007*, pp. 1-5. IEEE, 2007.

[70] M. Ben Slima, Roman Z. Morawski, and Andrzej Barwicz. "Spline-based variational method with constraints for spectrophotometric data correction." *IEEE transactions on instrumentation and measurement* 41, no. 6 (1992): 786-790.

[71] Felix Scholkmann, Jens Boss, and Martin Wolf. "An efficient algorithm for automatic peak detection in noisy periodic and quasi-periodic signals." *Algorithms* 5, no. 4 (2012): 588-603.

[72] Roman Z. Morawski, M. Ben Slima, M. S. Milewski, and Andrzej Barwicz. "Application of a digital signal processor for correction of spectrophotometric measurements." *IEEE transactions on instrumentation and measurement* 42, no. 3 (1993): 778-782.

[73] Pierre Brouard, Roman Z. Morawski, and Iand Andrzej Barwicz. "DSP-based correction of spectrograms using cubic splines and Kalman filtering." In *Instrumentation and Measurement Technology Conference, 1994. IMTC/94. Conference Proceedings. 10th Anniversary. Advanced Technologies in I & M., 1994 IEEE*, pp. 1443-1446. IEEE, 1994.

[74] Coleman Thomas, Mary Ann Branch, and Andrew Grace. *Optimization Toolbox for Use with MATLAB: User's Guide, Version 2*. Math Works, Incorporated. 1999.

[75] Krauss Thomas P., Loren Shure and John N. Little. "Signal Processing Toolbox for use with MATLAB". 1994.

[76] Katrin Schmitt, Kerstin Oehse, Gerd Sulz, and Christian Hoffmann. "Evanescent field sensors based on tantalum pentoxide waveguides–a review." *Sensors* 8, no. 2 (2008): 711-738.

[77] http://www.owls-sensors.com/sensorchip_ow2400, Optical Waveguide Grating Coupler, © 2000-2013 MicroVacuum Ltd [accessed Nov 18 2015].

[78] Kurt Tiefenthaler, Veronique Marie Briguet, E. Buser, M. Horisberger, and W. Lukosz. "Preparation of planar optical SiO2-TiO2 and LiNbO3 waveguides with a dip coating method and an embossing technique for fabricating grating couplers and channel waveguides." In *1983 International Techincal Conference/Europe*, pp. 165-173. International Society for Optics and Photonics, 1983.

[79] http://refractiveindex.info/download/data/2012/schott_optical_glass_collection_datasheets_dec_2012_us.pdf [accessed Nov 18 2015].

[80] https://www.aptina.com/support/Devsuite.jsp, DevWare, © 2008 - 2013 Aptina Imaging Corporation [accessed Oct 20 2013].

[81] Interfaces, MATLAB External. "The MathWorks." *Inc., www. mathworks. com* . 2005.

[82] http://www.mathworks.com/help/matlab/ref/polyfit.html, MATLAB®, © COPYRIGHT 1984–2013 by The MathWorks, Inc [accessed Nov 18 2015].

[83] http://www.opticsbalzers.com/en/326/Gratings-&-PWGs.htm, © Optics Balzers [accessed Nov 18 2015].

[84] http://www.cytodiagnostics.com/store/pc/Fluorescent-Nanocrystalsc17.htm, © 2015 Cyto-diagnostics Inc [accessed Nov 18 2015].

[85] Stefan Kedenburg, Marius Vieweg, Timo Gissibl, and Harald Giessen. "Linear refractive index and absorption measurements of nonlinear optical liquids in the visible and near-infrared spectral region." *Optical Materials Express* 2, no. 11 (2012): 1588-1611.

[86] Sergio B Mendes, and S. Saavedra. "On probing molecular monolayers: a spectroscopic optical waveguide approach of ultra-sensitivity." *Optics express* 4, no. 11 (1999): 449-456.

ABSTRACT

DENSE PERIODICAL PATTERNS IN PHOTONIC DEVICES: TECHNOLOGY FOR FABRICATION AND DEVICE PERFORMANCE

by

SABARISH CHANDRAMOHAN

December 2016

Advisor: Dr. Ivan Avrutsky

Major: Electrical Engineering

Degree: Doctor of Philosophy

For the fabrication, focused ion beam parameters are investigated to successfully fabricate dense periodical patterns, such as gratings, on hard transition metal nitride such as zirconium nitride. Transition metal nitrides such as titanium nitride and zirconium nitride have recently been studied as alternative materials for plasmonic devices because of its plasmonic resonance in the visible and near-infrared ranges, material strength, CMOS compatibility, and optical properties resembling gold. Coupling of light on the surface of these materials using sub-micrometer gratings gives additional capabilities for wider applications. Here we report the fabrication of gratings on the surface of zirconium nitride using gallium ion 30keV dual beam focused ion beam. Scanning electron microscope imaging and atomic force microscope profiling is used to characterize the fabricated gratings. Appropriate values for FIB parameters such as ion beam current, magnification, dwell time, and milling rate are found for successful milling of dense patterns on zirconium nitride.

For the device performance, a real-time image-processing algorithm is developed to enhance the sensitivity of an optical miniature spectrometer. The novel approach in this design is

the use of real-time image-processing algorithm to average the image intensity along the arc shaped images registered by the monochromatic inputs on the CMOS image sensor. This approach helps to collect light from the entire arc and thus enhances the sensitivity of the device. The algorithm is developed using $SiTiO_2$ planar waveguide. The accuracy of the mapping from *x*-pixel number scale of the CMOS image sensor to the wavelength spectra of the miniature spectrometer is demonstrated by measuring the spectrum of a known LED source using a conventional desktop spectrometer and comparing it with the spectrum measured by the miniature spectrometer. The sensitivity of miniature spectrometer is demonstrated using two methods. In the first method, the input laser power is attenuated to 0.1 nW and the spectra is measured using the miniature spectrometer. Even at low input power of 0.1nW, the spectrum of monochromatic inputs is observed well above the noise level. Second method is by quantitative analysis, which measures the absorption of CdSeS/ZnS quantum dots drop casted between the gratings of Ta_2O_5 planar single-mode waveguide. The expected guided mode attenuation introduced by monolayer of quantum dots is found to be approximately 11 times above the highest noise level from the absorption measurements. Thus, the miniature spectrometer is capable of detecting the signal from the noise level even with the absorption introduced by monolayer of quantum dots.

AUTOBIOGRAPHICAL STATEMENT

Sabarish Chandramohan received his Bachelor of Technology in Electronics and Communication Engineering from University of Kerala, Kerala, India in May 2006. He worked as L1-engineer (Access Corporate NOC) at Tata Communications Limited in Bangalore, Karnataka, India and 4G WiMAX implementation engineer at Tata Communications Limited in Kochi, Kerala, India . He received his Master of Science in Electrical Engineering from Wayne State University in August 2014. His Master's Thesis was titled "REAL-TIME HIGH RESOLUTION INTEGRATED OPTICAL MICRO-SPECTROMETER". He received the Wayne State University's Graduate Professional Scholarship during the academic year 2011-2012, while pursuing his Master's degree. He is now pursuing his PhD in Electrical Engineering at Wayne State University under the guidance of Dr. Ivan Avrutsky. He was a member of Optical Society of America and IEEE Signal Processing Society and was a member of Microwave Society and COMSOC of IEEE.